Investigation of Transmon Qubit Designs
-A Study of Plasma Frequency Predictability

Philip Krantz

Investigation of transmon qubit designs
-A study of plasma frequency predictability
Thesis for the degree Master of Science in Nanoscale Science and Technology
PHILIP KRANTZ

Diploma work performed at:
Quantum Device Physics Laboratory
Department of Microtechnology and Nanoscience
Chalmers University of Technology
SE-412 96 Gothenburg, Sweden
Telephone:+46 (0)31 772 1000

Supervisor and examiner:
Prof. Per Delsing
Quantum Device Physics Laboratory
Department of Microtechnology and Nanoscience
Chalmers University of Technology
SE-412 96 Gothenburg, Sweden
Telephone:+46 (0)31 772 3317

Abstract

This master thesis was dedicated to design, fabricate, and characterize subsystems of superconducting transmon qubits for future quantum computers. Focus was on investigating the predictability of the plasma frequency of the transmon. This is especially important in multi-qubit circuits so that the frequencies of the qubits can be evenly distributed over the available frequency spectrum. The plasma frequency is governed by the normal state resistance of the two Josephson junctions along with the total capacitance of the transmon. In previous experiments, this frequency predictability relied entirely upon successful simulations of the system. However, even small simulation errors prove to generate severe consequences for the system and a better, more systematic control is desired.

In order to identify and minimize this uncertainty, subsystems of the transmon were isolated and investigated. Test structures were fabricated and used to measure the normal state resistance of tunnel junctions with different areas and oxidation parameters using a four-point probe setup. A regime within which the reproducibility is increased was statistically identified. The shunt capacitance, *i.e.* the largest contribution to the total capacitance, of transmons was extracted by coupling identical capacitors to resonators. The coupling capacitance of a resonator is related to its external quality factor which was measured from analyzing the reflected microwave signal at cryogenic temperatures.

The smallest standard deviation of normal state resistances for 110 junction pairs was measured for junctions with an area $\geq 2.37\ \mu m^2$ to be 1.48 %, corresponding to an uncertainty contribution of 44.4 MHz for a designed plasma frequency of 6 GHz. Six resonators were measured throughout the shunt capacitance experiment and a linear fit was used to compare the results with a written model based on conformal mapping.

List of Figures

Symbols and abbreviations

$\mathbf{A}$	Vector potential
α_r	Relative anharmonicity
c	Speed of light
C_Σ	Total qubit capacitance
C_c	Coupling capacitance
C_r	Resonator capacitance
C_s	Shunt capacitance
C_J	Josephson junction capacitance
C_g	Gate capacitance
C_l	Capacitance per unit length
CPW	Coplanar Waveguide
δ_0	Average phase
Δ	Superconducting gap
e	Electron charge
E_J	Josephson energy
E_C	Charging energy
E_m	Energy of level m
ε_m	Charge dispersion of level m
ϵ_{eff}	Effective dielectric constant
ϵ_r	Dielectric constant
f_0	Resonance frequency of resonator
ϕ, θ	Spherical coordinate angles
Φ	Magnetic flux
Φ_0	Magnetic flux quanta
Φ_{ext}	External magnetic flux
φ	Quantum mechanical phase
G	Gap width
Γ	Pathway
h,$\hbar$	Planck,Dirac constant
$\hat{H}$	Hamiltonian
$\hat{\mathbf{I}}$	Identity matrix
I_s	Super-current
I_c	Critical current
I_{tot}	Total current over junctions
l	Length of resonator
L_l	Inductance per unit length
n	Number of Cooper-pairs
n_g	Reduced gate charge
Ψ	Quantum state of qubit
$\Psi(\mathbf{r})$	Wave function of Cooper-pairs
P_{ox}	Oxidation pressure
Q_{ext}	External quality factor
Q_{int}	Internal quality factor
Q_{tot}	Total quality factor
R_N	Normal state resistance
R_Q	Quantum resistance
$\rho(\mathbf{r})$	Charge density
$\hat{\rho}$	Density operator
$\hat{\sigma}_{x,y,z}$	Pauli matrices
$\hat{\sigma}$	Pauli operator
$\mathbf{s}$	Bloch vector
t	Thickness of Al film
t_{ox}	Oxidation time
T_c	Critical temperature
V	Voltage over Josephson junction
V_g	Gate voltage
W	Width of transmon qubit
Z_0	Load impedance
Z_c	Characteristic impedance

Acknowledgements

There are many people whom I would like to thank for a lot of assistance and support throughout this project.

First of all, I would like to thank my supervisor Prof. Per Delsing for giving me the great opportunity of doing my master thesis project in such an encouraging and friendly environment.

Many thanks to ...

... Martin Sandberg and Fredrik Persson for being so supportive and tolerant to me during my training in the clean room and throughout all fruitful discussions.

... Chris Wilson for everything you have taught me during my project regarding all topics from circuit designs to fabrication.

... Thilo Bauch for all the hours you spent training me in the low-temperature laboratory with the Heliox cryostat. I really appreciate your supportive attitude in helping me to get familiar with the system. Thank you!

... Niclas Lindvall for all the hours you spent helping me with the e-beam lithography and also all nice coffee breaks we had throughout the past year.

... Tine Greibe, Martin Gustafsson and Henrik Fredriksen for many fruitful discussions regarding fabrication recipes and tips in the clean room.

... Arsalan Pourkabirian, Michael Simoën, Chloé Bureau-Oxton, IoChun Hoi, Tauno Palomaki, Shahid Newaz, Sebastian de Graaf, Samuel Lara Avila, Simon Abay Gerbrehiwot, Andreas Myrin, Jan Jacobsson, Staffan Pehrson and Ann-Marie Frykestig and the rest of QDP for a lot of help and support.

Finally, thanks to my girlfriend Annika for being so wonderful and understanding, even when I come home from the clean room in the middle of the night.

Contents

Chapter 1

Introduction

The system that is discussed in this thesis consist of a tunable superconducting cavity and a number of quantum bits of the so called transmon type placed in the cavity. The specific aim of this thesis has been to improve reproducibility and predictability of the quantum bits.

The intention of this chapter is to introduce the reader to fundamental concepts on which the transmon qubit is based.

1.1 Quantum computation

In 1982, Richard Feynman proposed[1] an alternative of using classical computers to simulate systems of quantum mechanical nature. He argued that this could be done with greater efficiency using a processor whose architecture, in itself, is based on the laws of quantum mechanics. This *quantum computer* should operate following the fundamental principles of quantum mechanics, such as superposition and entanglement. Similar to a classical computer, a quantum processor consists of wires and logical gates. However, as opposed to the computer on which this report is written, a quantum computer utilizes the quantum mechanical properties of the system to represent the information as well as performing operations.

The fundamental element of a quantum computer is the quantum bit (qubit). As opposed to a classical bit that constitutes the memory element of an ordinary classical computer, a qubit can not only represent the two classical states zero and one, but also a quantum superposition of the two states. So far, several categories of qubit systems have been proposed[2][3] and demonstrated[4][5]. This master thesis project has been dedicated to investigate one promising quantum processor architecture, namely superconducting qubits coupled to resonant cavities.

This branch of physics has evolved with inspiration from quantum optics and the techniques within nanofabrication allowing to create quantum optics experiments on a chip instead of using lasers and crystals. The microwave photons are confined inside a cavity with small 1D mode volume, which together with the large dipole moment of the qubit allows the interaction between the qubit and the cavity to enter into the strong coupling regime. This area of quantum physics is known as circuit Quantum Electrodynamics (circuit QED)[6] and is promising for quantum computation as well as studying more fundamental physical phenomena such as the interaction between microwave photons and artificial atoms.

1.1.1 Quantum bits versus classical bits

The difference between a bit and a qubit is that the latter can be found in a state other than $|0\rangle$ and $|1\rangle$, namely in a linear superposition of the two states which in Dirac notation can be written as

$$|\Psi\rangle = \alpha|0\rangle + \beta|1\rangle, \qquad |\alpha|^2 + |\beta|^2 = 1 \tag{1.1}$$

where α and β are complex numbers. From fundamental quantum mechanics [7], it is known that all two-level systems can be described in terms of the Pauli matrices

$$\hat{\sigma}_1 = \hat{\sigma}_x = \begin{pmatrix} 0 & 1 \\ 1 & 0 \end{pmatrix} \quad \hat{\sigma}_2 = \hat{\sigma}_y = \begin{pmatrix} 0 & -i \\ i & 0 \end{pmatrix} \quad \hat{\sigma}_3 = \hat{\sigma}_z = \begin{pmatrix} 1 & 0 \\ 0 & -1 \end{pmatrix} \tag{1.2}$$

satisfying the commutation relation

$$[\hat{\sigma}_i, \hat{\sigma}_j] = 2i\varepsilon_{ijk}\hat{\sigma}_k, \tag{1.3}$$

where

$$\varepsilon_{ijk} = \begin{cases} +1 & \text{if } (i,j,k) = (1,2,3)... \\ -1 & \text{if } (i,j,k) = (1,3,2)... \\ 0 & \text{otherwise} \end{cases}$$

Now, the statistical quantum state can be described in terms of the density operator of the system defined as

$$\hat{\rho} = \frac{1}{2}\left(\hat{I} + \mathbf{s}\cdot\hat{\sigma}\right) \tag{1.4}$$

where $\hat{\sigma} = \hat{\sigma}_1\hat{x} + \hat{\sigma}_2\hat{y} + \hat{\sigma}_3\hat{z}$ is the Paulioperator and $\mathbf{s}$ is the Bloch vector. For a pure quantum state $\hat{\rho} = |\Psi\rangle\langle\Psi|$, the Bloch vector has unit length $\left(\sum_i |s_i|^2 = 1\right)$ and points on the surface of a unit sphere known as the Bloch sphere. The spherical coordinate angles θ and ϕ can be used to describe any state $|\Psi\rangle$ of the qubit onto the Bloch sphere[1], see Fig. 1.1.

$$|\Psi\rangle = \cos\left(\frac{\theta}{2}\right)|0\rangle + e^{i\phi}\sin\left(\frac{\theta}{2}\right)|1\rangle \tag{1.5}$$

where $|\cos(\theta/2)|^2$ and $|\sin(\theta/2)|^2$ are the probabilities of measuring the qubit in state $|0\rangle$ or $|1\rangle$, respectively.

An essential part of quantum computation is the read-out of the state. But according to Heisenberg's uncertainty principle, a consequence of measuring the state of a quantum mechanical system is to gradual collapse the state *i.e.* the system decohers during the measurement. On the Bloch sphere, this operation will result in a projection of the state onto the z-axis if the measurement basis is σ_z. Once the vector has left the sphere surface, the quantum state is no longer pure but mixed. The shorter **s** becomes, the state evolves into a more classical state until eventually the vector length is zero. Then the system is in a maximum mixed state corresponding to a classical state at the center of the Bloch sphere. For a more elaborative description of the Bloch formalism for quantum information, the reader is referred to [8].

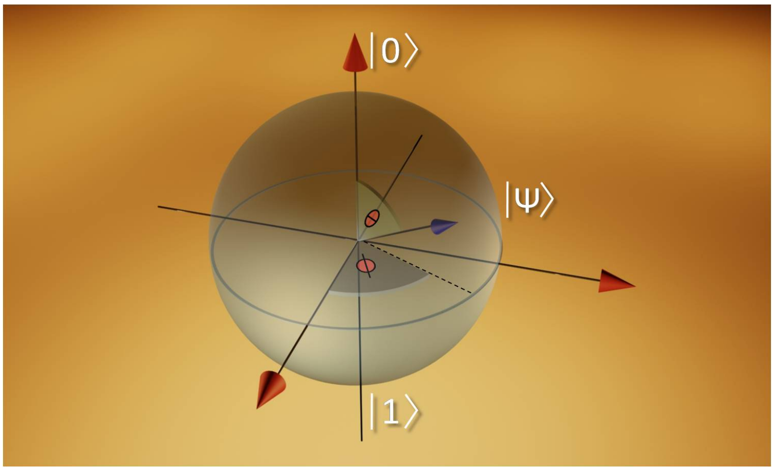

Figure 1.1: *An animated Bloch sphere illustrating a general pure quantum state $|\Psi\rangle$ as a unit vector, pointing on the surface of the sphere. States $|0\rangle$ and $|1\rangle$ are found on the north and south poles of the sphere, respectively.*

---

[1] The Bloch sphere is not a way to illustrate the visual appearance of the system, but rather an aid to get an intuition about the present state of the qubit as well as how it responds to operations.

1.2 Superconducting devices

In 1911, H.K. Onnes first discovered that the resistance of mercury dropped to zero when cooled below a critical temperature, T_c [9]. This phenomenon was named superconductivity and has ever since then been subject of research all over the world. In his lectures on physics, Feynman discusses in short terms the origin to why superconductivity is observed for many metals [10]. The interaction between the electrons in the metal and the vibrations of its atom lattice give rise to small effective attraction between the electrons. Therefore, it is energetically favorable for the electrons to form pairs. This has the remarkable effect that the electrons, which are Fermi particles, will become Bose particles (bosons) as they appear in pair. The electron pairs, known as Cooper-pairs, carry the property that if a large number of pairs are occupying the same energy state, so will nearly all other pairs. Now, due to the fact that the superconducting state of a metal takes place at very low temperatures, almost all Cooper-pairs will be bound to stay in their lowest energy state. This electron-electron bond is, however, very weak and is therefore easily broken if only a small thermal energy act on it. Hence, when $T < T_c$ the electrons move in pairs and when $T > T_c$ no pairs are formed and normal electrons flow in the metal. The wave function of the Cooper-pairs in their lowest energy state can be written

$$\psi(\mathbf{r}) = \sqrt{\rho(\mathbf{r})}\mathbf{e}^{\mathbf{i}\varphi(\mathbf{r})} \tag{1.6}$$

where ρ is the charge density and φ is the quantum mechanical phase.

Superconductivity has made it possible to create new interesting physics in devices whose properties are govern by the tunneling of these Cooper-pairs through barriers. In particular, this allows for the creation of non-linear circuit elements which, as opposed to the harmonic oscillator, have energy spectra where the level splitting varies between different energy levels. This feature has proven to be necessary for the realization of effective two-level systems where the two lowest energy levels are separated from the higher states.

These devices can be used to create artificial atoms at the mesoscopic scale exhibiting quantum phenomenons even though these are not of single atom size.

1.2.1 The Josephson effects

In 1962, Brian Josephson made a pioneering theoretical prediction about superconductors [11]. He concluded that if two superconductors were put in close vicinity of each other forming a weak link (see Fig. 1.2), a zero-voltage tunneling current (called a super-current) of Cooper pairs could still flow through the junction [12]. This super-current is given as

$$I_s = I_c \sin(\varphi) \tag{1.7}$$

where $\varphi = \varphi_2 - \varphi_1$ is the phase difference between the two superconducting electrodes and I_c is the critical current, *i.e.* the maximum super-current that the junction can support. The relation for the super-current in (1.7) is known as *Josephson's first relation.* Furthermore, Josephson predicted that if a voltage was built up across the junction, the phase φ would evolve in time according to the following relation

$$\frac{d\varphi}{dt} = \frac{2e}{\hbar}V \tag{1.8}$$

meaning that the current would now be an alternating current of amplitude I_c and frequency $\nu = \frac{2e}{h}$. Thus, the energy $E = h\nu$ equals the amount of energy required to transfer a Cooper pair across the junction. The voltage relation in (1.8) is known as *Josephson's second relation.*

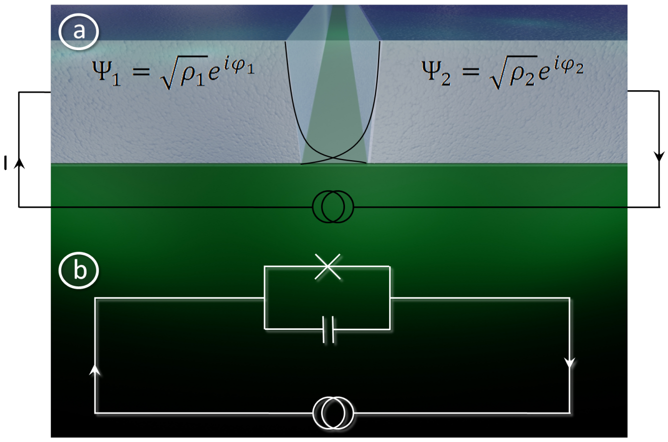

Figure 1.2: ***a)*** *An animated Josephson junction where two superconducting electrodes of aluminum are separated by a thin insulating oxide. When biasing the junction, the Cooper-pairs on the two electrodes are described by the wave functions Ψ_1 and Ψ_2, respectively. If the oxide is made thin enough, an overlap of the wave functions give rise to quantum mechanical tunneling of Cooper-pairs.* ***b)*** *The circuit diagram symbol often used for the Josephson junction.*

In their superconducting state, the Cooper-pairs form a condensate on each superconductor, which means that the electrons will be in their lowest energy state and are therefore described by the same wave function. From the fundamental concept of quantum mechanical tunneling it follows that if the two superconductors are separated by nothing but a weak-enough link, the wave functions from the two sides will have an overlap, *i.e.* interact with each other, see Fig. 1.2 a). For further reading, see *e.g.* [13].

Josephson junctions can be fabricated in many different ways, using many different materials. In the context of this thesis project, the Josephson junctions consist of two electrodes of superconducting aluminum separated by a thin insulating oxide.

1.2.2 The dc-SQUID

The main device from which the tunable cavity, as well as, its embedded transmon qubits are constructed is the dc Superconducting QUantum Interference Device, (dc-SQUID) [12]. It consists of two superconductors separated by two Josephson junctions which together form a loop, see Fig. 1.3.

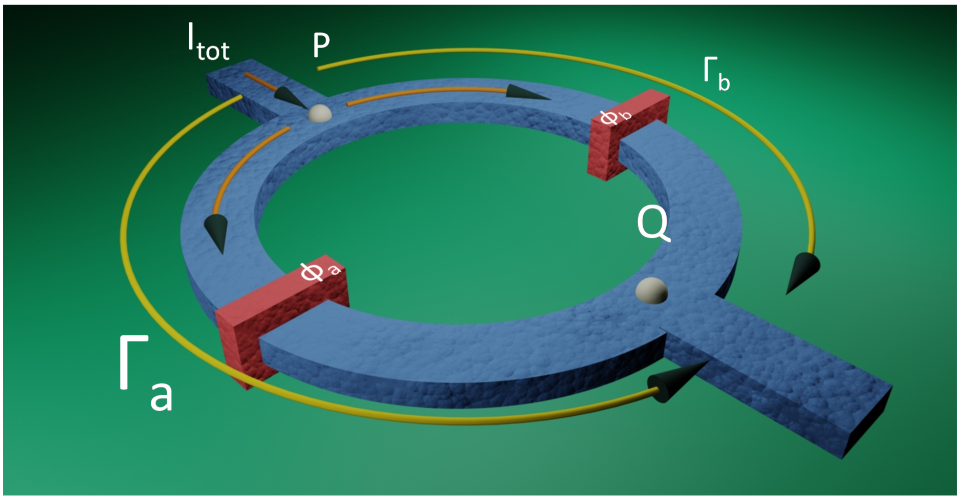

Figure 1.3: *A schematic animation of the dc-SQUID. The two superconductors are separated by two Josephson junctions. The two pathways between point P and Q are denoted* Γ_a *and* Γ_b *and the phase differences between the two sides of each junction,*φ_a *and* φ_b.

The dc-SQUID can be characterized through the maximum amount of current that can flow through the two junctions, *i.e.* from point P to point Q. To derive the critical current of the device, first consider the phases for the two pathways Γ_a and Γ_b, given as

$$\varphi_{P_a \to Q_a} = \varphi_a + \frac{2e}{\hbar}\int_{\Gamma_a} \mathbf{A}\cdot\mathbf{ds} \qquad \varphi_{P_b \to Q_b} = \varphi_b + \frac{2e}{\hbar}\int_{\Gamma_b} \mathbf{A}\cdot\mathbf{ds} \tag{1.9}$$

Moreover, the difference in phase between the two paths must be zero, giving

$$\varphi_a + \frac{2e}{\hbar}\int_{\Gamma_a} \mathbf{A}\cdot\mathbf{ds} - \varphi_b - \frac{2e}{\hbar}\int_{\Gamma_b} \mathbf{A}\cdot\mathbf{ds} = 0 \tag{1.10}$$

$$\varphi_a - \varphi_b = \frac{2e}{\hbar}\int_{\Gamma_b} \mathbf{A}\cdot\mathbf{ds} - \frac{2e}{\hbar}\int_{\Gamma_a} \mathbf{A}\cdot\mathbf{ds} = \frac{2e}{\hbar}\oint_{\Gamma} \mathbf{A}\cdot\mathbf{ds} = \frac{2e\Phi}{\hbar} \tag{1.11}$$

Now, the phase shifts over the two junctions can be expressed on the form

$$\varphi_a = \delta_0 + \frac{e\Phi}{\hbar}, \qquad \varphi_b = \delta_0 - \frac{e\Phi}{\hbar} \tag{1.12}$$

where $\delta_0 = \frac{\varphi_a+\varphi_b}{2}$ denotes the average phase. From the first Josephson relation (1.7) and assuming identical junctions it follows that the total current can be written

$$I_{tot} = I_c\left(\sin\left(\delta_0 + \frac{e\Phi}{\hbar}\right) + \sin\left(\delta_0 - \frac{e\Phi}{\hbar}\right)\right) = 2I_c \sin\delta_0 \cos\left(\frac{e\Phi}{\hbar}\right) \tag{1.13}$$

$$I_c^{max} = 2I_c\left|\cos\left(\frac{\pi\Phi}{\Phi_0}\right)\right| = I_c^{\mathrm{SQUID}}(0)\left|\cos\left(\frac{\pi\Phi}{\Phi_0}\right)\right| \tag{1.14}$$

where $\Phi_0 = \frac{h}{2e} \approx 2\cdot 10^{-15}$ Wb is the magnetic flux quantum. In Fig. 1.4, the modulation of critical current of the dc-SQUID is plotted as a function of the applied magnetic flux, Φ/Φ_0

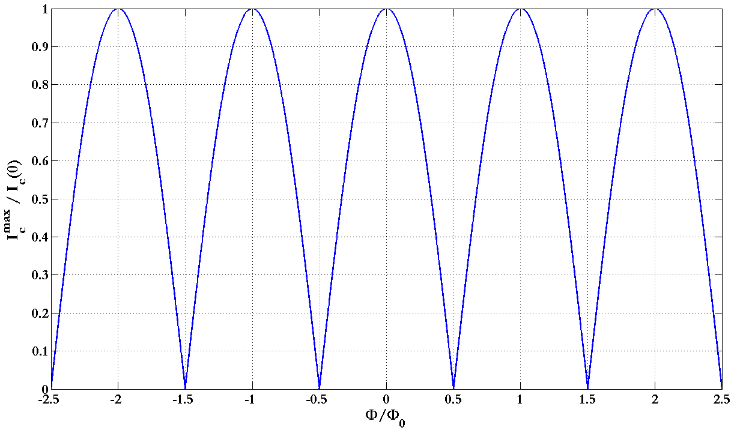

Figure 1.4: *The modulation of the critical current $I_c^{max}/I_c(0)$ of the dc-SQUID as function of the applied magnetic field through the loop Φ/Φ_0.*

1.3 Motivation and project objectives

Motivation

The overall objective of this master thesis project is to be able to predict the plasma frequency, ν_p of a transmon qubit *i.e.* the difference in frequency between the ground- and the first excited states of the system. In previous experiments, see [23], the plasma frequency of transmons have successively been tuned through an external magnetic field in close vicinity to the transmons. This technique, however, leads to several drawbacks, including...

1. ... a decreased ratio of Josephson energy and charging energy, E_J/E_C, which could result in that the transmon ends up outside of the transmon regime ($E_J/E_C \gtrsim 20$).
2. ... entrapment of magnetic flux in the thin film, leading to a decreased quality factor of the resonator.
3. ... inconvenience of placing a magnet in the close vicinity of the transmon. The inconvenience would scale with the number of transmons.
4. ... increased complexity for a potential future up scale of the system, as each new transmon would lead to an increased complexity of managing the transmon tuning accurately.

If the transmons could be designed with sufficient precision of ν_p *i.e.* within an error margin of $|\Delta\nu_p| \approx 50$ MHz, there would be no need to tune the transmons using a magnetic field. This would facilitate a future upscale of the system as more transmons would fit within the tuning range of the cavity.

Project objectives

The plasma frequency of the qubit is set by its Josephson junction resistance R_N and its total capacitance, C_Σ. The objectives of the project can be divided into following parts:

1. Investigate R_N for various junction dimensions of the transmon.
2. Investigate quantitatively the reproducibility of the junction size and their fabrication yield.
3. Measure the shunt capacitance C_s of a promising design and compare it to modeled values.
4. Find the reproducibility of the plasma frequency of the transmons.

Chapter 2

Theoretical background

The aim of this chapter is to introduce the reader to the transmon qubit as well as the resonant cavity used to operate the system.

2.1 From the Cooper-Pair box to the transmon

2.1.1 The Single Cooper-Pair Box

The story of the Transmon qubit is best told by first briefly considering its ancestor from which it was derived; the Single Cooper-pair Box (SCB) [14] [15] [16]. The SCB consists of a small aluminum island, connected to a superconducting reservoir through a Josephson junction on one side and biased by a gate capacitance C_g and a gate voltage V_g on the other side, see Fig.2.1 a). When the junction is in its superconducting state, Cooper pairs can tunnel to and from the island. The potential of the island can be controlled through the gate voltage. The SCB is characterized by two energies, the Josephson energy and the Coulomb energy of the Cooper pair given as

$$E_J = \frac{R_Q \Delta}{2R_N}, \qquad R_Q = \frac{h}{4e^2} \tag{2.1}$$

$$E_C = \frac{e^2}{2C_\Sigma}, \qquad C_\Sigma = C_g + C_J \tag{2.2}$$

where R_Q and R_N are the quantum and normal state resistances, respectively. Δ is the superconducting energy gap related to the critical temperature of the material[1] and C_Σ represents the total capacitance between the island and its circuit

---

[1] The critical temperature for bulk aluminum is $T_c = 1.176$ K [17]. However, the effective critical temperature for a thin film is slightly higher than for bulk material. According to BCS theory [18], $\Delta = 1.76 k_b T_c$.

environment. In addition the system is characterized by the reduced gate charge $n_g = C_g V_g/2e$. If another Josephson junction is added in parallel to the first one, these form a dc-SQUID with the property of a tunable E_J (recall Fig. 1.4) by means of an external magnetic field Φ_{ext} through its loop, see Fig. 2.1. The effective Josephson energy is then given as

$$E_J = E_J^{max} \left| \cos \left(\frac{\pi \Phi_{ext}}{\Phi_0} \right) \right| \tag{2.3}$$

where $\Phi_0 = h/2e$ is the flux quantum. Further information about the SQUID can be found in *e.g.* [13]. The Hamiltonian of the SCB can now be written in terms of these two energies in the charge basis

$$\hat{H}_{SCB} = 4E_C \sum_{n=-\infty}^{\infty} (\hat{n} + n_g)^2 |n\rangle\langle n| - \frac{E_J}{2} \sum_{n=-\infty}^{\infty} \left[|n+1\rangle\langle n| + |n\rangle\langle n+1| \right] \tag{2.4}$$

By doing the transformation $\hat{n} \rightarrow -i\frac{d}{d\phi}$ the Hamiltonian takes the form of a quantum rotor in phase space

$$\hat{H}_{SCB} = 4E_C(-i\frac{d}{d\phi} + n_g)^2 - E_J \cos\phi \tag{2.5}$$

The exact solutions to the Hamiltonian in equation (2.5) are obtained using Mathieu functions [5] and are plotted in Fig. 2.2.

In order to operate the SCB as a qubit it is essential that it can be considered a two-level system, *i.e.* the two lowest eigenenergies must be well-separated from any higher energy levels of the system. In Fig. 2.2 a) the charge dispersion relations for the three lowest eigenenergies are plotted as a function of the reduced gate charge n_g and E_J/E_C. The bands form a periodic structure where the energy required for transitions between the ground state $|0\rangle$ and the first excited state $|1\rangle$ is smallest when the gate charge $n_g = m + \frac{1}{2}$. In 2002, Vion *et al.* [19] demonstrated that these so called *sweet spots* serve as optimal working points to operate the qubit.

The SCB is mainly characterized by the ratio E_J/E_C. The two limiting regimes where $E_J/E_C \ll 1$ and $E_J/E_C \gg 1$ are referred to the *charge*- and *phase* limits, respectively. However, even though the goal of obtaining an effective two-level system is fulfilled, the SCB has one major drawback in its dependence of keeping the charge constant at the sweet spot, indicated in Fig. 2.2 b). Due to the environment, the qubit will be subject to fluctuations of the gate charge, known as charge noise. This means that the level spacing between the two levels will fluctuate and lead to short coherence times of the qubit. In the Bloch representation (recall Fig. 1.1), these fluctuations will lead to that $|\mathbf{s}|$ decreases.

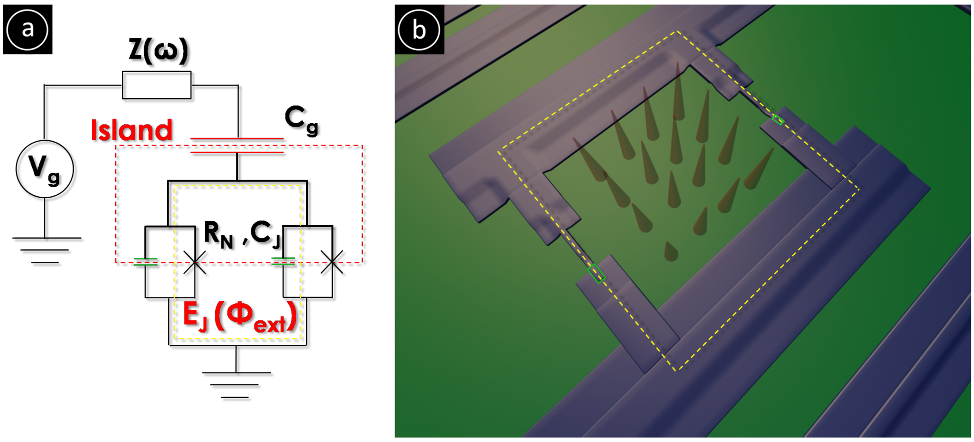

Figure 2.1: ***a)*** *The circuit diagram of the single Cooper Pair Box. The island is biased with a gate voltage V_g through a gate capacitance C_g and separated from the reservoir by two parallel Josephson junctions.* ***b)*** *An animated cartoon of an applied magnetic field through the SQUID-loop of the qubit.*

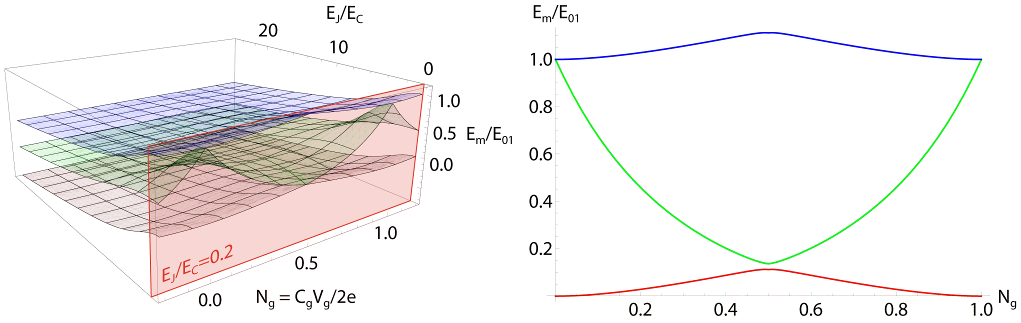

Figure 2.2: *The surface plot shows the eigenenergies E_m/E_{01} for the three lowest energy bands of the Hamiltonian for the qubit (2.5) as a function of the effective offset charge n_g and the ratio E_J/E_C. b) A cross-section showing a sweet spot at $n_g = 0.5$ in the charge regime $E_J/E_C \ll 1$. The Josephson energy results (for $E_J/E_C \ll 1$) in an energy splitting of the order of E_J between E_0 and E_1.*

2.1.2 Entering into the transmon regime

To solve the problem of sensitivity to charge noise, the transmon qubit was proposed by Koch *et al.* [5] and is a new and improved version of the SCB. The modification that was made was to design the qubit to have a much lower E_C. This is obtained by increasing the sizes of the two islands, thus introducing a dominant capacitance in parallel with the two Josephson junctions. This means that E_J/E_C is taken away from the charge limit and instead entering a new regime, known as the transmon regime. In addition to the energy ratio E_J/E_C, the transmon can be characterized by its plasma frequency ν_p defined as

$$\nu_p = \frac{\sqrt{8E_JE_C}}{h} \tag{2.6}$$

related to the transition between $|0\rangle$- and $|1\rangle$ states of the transmon through

$$E_{01} = h\nu_p - E_C \tag{2.7}$$

To motivate this parameter modification, two essential quantities need to be introduced in the energy band diagram in Fig. 2.2, namely the charge dispersion and the relative anharmonicity. The charge dispersion is defined as $\epsilon_m = E_m(n_g = \frac{1}{2}) - E_m(n_g = 0)$, *i.e.* the peak to peak value of the variation of eigenenergy of the mth level. It follows from Fig. 2.2 that the smaller the charge dispersion gets, the less the qubit frequency will change in response to gate charge fluctuations.

The relative anharmonicity is defined as the level spacing between the energy levels of the system and is given as $\alpha_r = (E_{12} - E_{01})/E_{01}$, where E_{01} and E_{12} are the energy level spacings of the system. Too small anharmonicity would lead to risk of exciting the system to higher energies and operations would have to be smaller. Thus, the transmon would no longer act as a qubit but rather a many-level system. Both the charge dispersion and the anharmonicity has a common dependence in the ratio of the Josephson and the Coulomb energies E_J/E_C. As Koch *et al.* derived, the charge dispersion decreases exponentially when E_J/E_C is increased and becomes almost flat when $E_J/E_C \gtrsim 20$. However, the prize to pay for the improved charge dispersion is that the anharmonicity of the energy levels also decreases. Fortunately, the latter has only a weak power dependence on E_J/E_C. Thus, it is possible to enter into a regime where the transmon is virtually insensitive to charge noise, maintaining a sufficiently large anharmonicity for the system to act as an effective two-level system. This range of $E_J/E_C \gtrsim 20$ for which the transmon has sweet spots everywhere is known as the transmon regime, see Fig. 2.3 b).

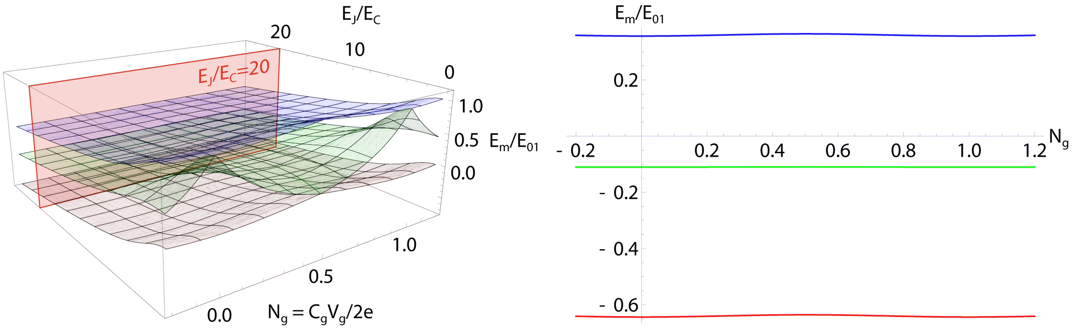

Figure 2.3: *As in Fig. 2.2, the surface plot shows the eigenenergies* E_m/E_{01} *for the three lowest energy bands of the Hamiltonian for the qubit (2.5) as a function of the effective offset charge* N_g *and the ratio* E_J/E_C. *b) A cross-section in the transmon regime* $E_J/E_C = 20$. *By increasing* E_J/E_C, *the energy levels become flat having sweet spots everywhere.*

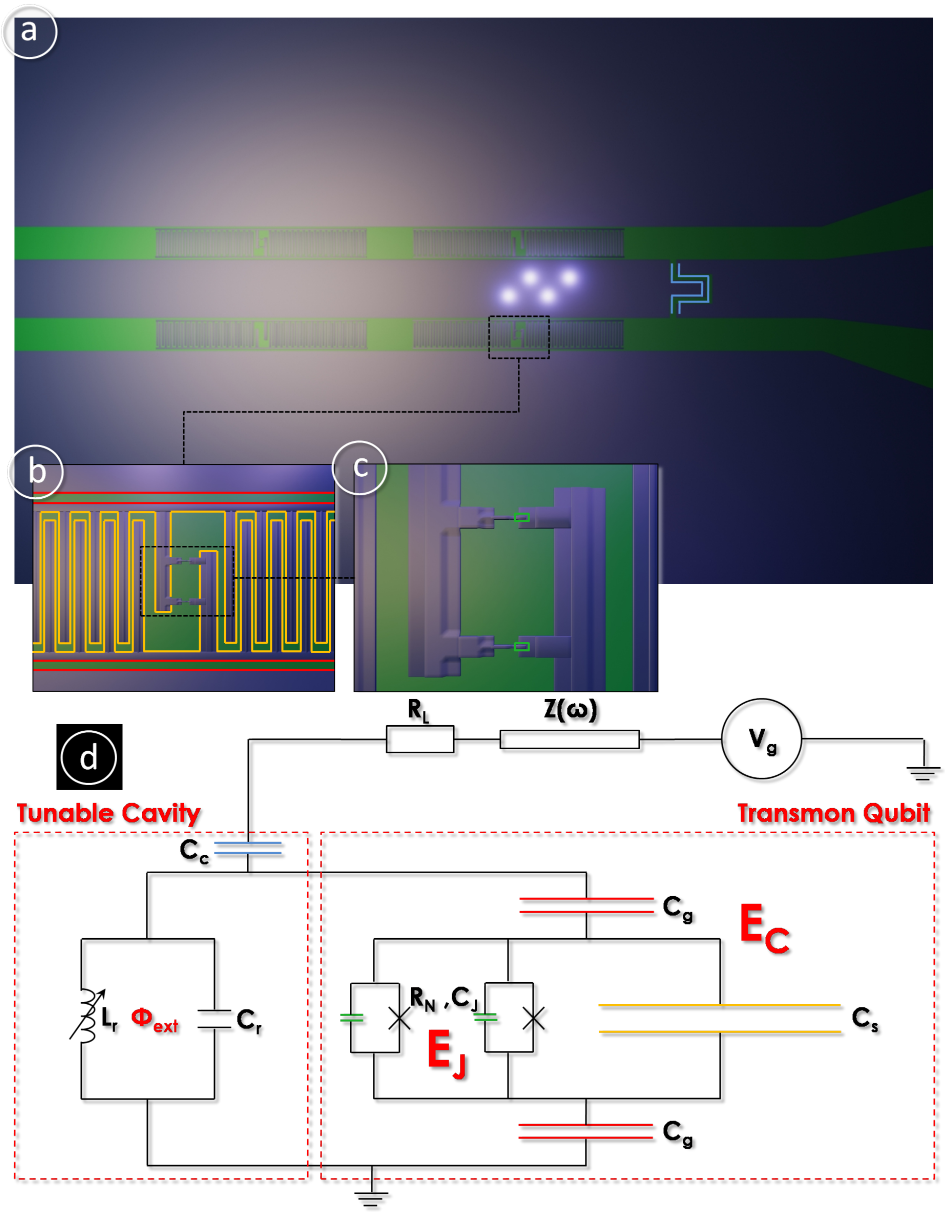

Figure 2.4: *A transmon coupled to a tunable cavity resonator.* ***a)*** *An animation illustrating the coupling between the cavity and the environment via a coupling capacitance* C_c *(in blue). In* ***b)*** *the capacitances to center strip/ground and the shunt capacitance of the transmon are illustrated in red and yellow, respectively.* ***c)*** *the center of the transmon consists of two Josephson junctions together with capacitance contribution,* C_J *(in green).* ***d)*** *A circuit diagram, divided into two boxes representing the tunable cavity and one of the transmons.* E_C *and* E_J *are governed by the design of the capacitors and junctions, respectively.* Φ_{ext} *represents the external magnetic field that is applied through the SQUID-loop that terminates the cavity, acting as a tunable inductance.*

2.2 Resonant cavities

A key element of circuit Quantum Electrodynamics is the microwave resonator cavity [20]; an element capable of storing energy which oscillates between electric and magnetic energy. In a resonant cavity, only certain standing electromagnetic waves *i.e. modes*, with discrete energies will be present. In addition, each mode can be occupied by a number of microwave photons, n. Confining microwave photons inside the one-dimensional cavity of small mode volume provides a strong coupling to the components coupled to it.

The cavity to which the transmon qubits will be coupled is a coplanar waveguide (CPW) transmission line. It consists of a center strip of width W, separated by a gap of width G from the ground planes on each side, see Fig. 2.5. This design was proposed by C.P. Wen in 1969 [21] and has an advantage over *e.g.* the microstrip line in the possibility to connect active and passive circuit components between the center strip to the ground planes. In addition, the CPW is suitable for microprocessing due to the high flexibility of materials and methods available for single layer structures. There are two important parameters for the cavity resonator, namely its resonance frequency f_0 and its quality factor Q_{tot}.

The resonance frequency for a quarter wavelength resonator is set by its length l through the relation

$$f_0 = \frac{c}{4l\sqrt{\varepsilon_{eff}}} \tag{2.8}$$

where c is the speed of light in vacuum and the additional design parameters along with the substrate properties are encountered for in the effective dielectric constant ε_{eff}.

The quality factor, or *Q-value*, of a resonator is defined as

$$Q = \frac{\text{Stored energy}}{\text{Dissipated energy / radian}} \tag{2.9}$$

The energy losses of the resonator are divided into two parts. First, the *internal Q-value* Q_{int}, accounts for the energy dissipated into the substrate (see the master thesis of Myrin [22]). Second, the *external Q-value* encounters for the energy lost to the external circuit connected to the resonator. The *total Q-value* can now be expressed in terms of these two contributions

$$Q_{tot} = \left(\frac{1}{Q_{int}} + \frac{1}{Q_{ext}}\right)^{-1} \tag{2.10}$$

The external Q-value can be designed by using a coupling capacitor, which reduces the energy loss out from the resonator and defines where the resonator starts, see

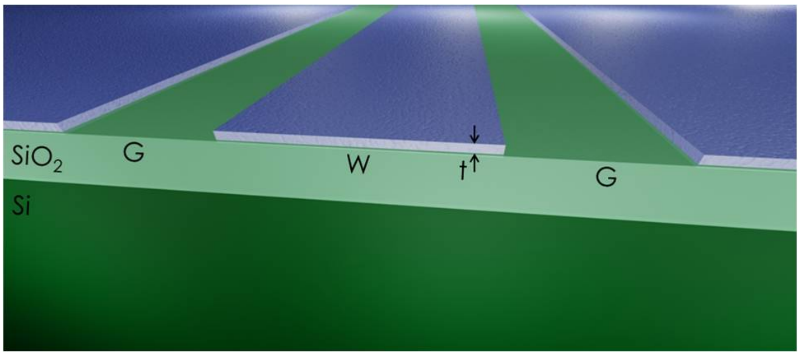

Figure 2.5: *An animated cross section cut of a coplanar waveguide cavity on top of a two-layered substrate, consisting of 400nm of wet grown oxide on top of a 380µm silicon wafer. The CPW has a center conductor strip with a width W and gaps of width G. The thickness of the metal is denoted t and is of the order of 100 nm.*

Fig. 2.6. The external Q-value is given as

$$Q_{ext} = \frac{(1 + (\omega_r C_c R_L)^2)(C_r + C_c)}{\omega_r C_c^2 R_L} \tag{2.11}$$

where $\omega_r = 2\pi f_0$ is the resonance frequency of the resonator, C_r is the capacitance between the center strip and the ground planes, C_c is the coupling capacitor, and R_L is the load resistance, recall Fig. 2.4. For a quarter-wavelength resonator, $C_r = \frac{C_l l}{2}$ [23], where C_l denotes the capacity per unit length. Whether it is desired to have a high or a low Q_{ext} depends entirely on the application of the device. In this project, the resonator is used merely as a tool to measure the shunt capacitance of the transmons by placing different interdigitated finger capacitors of unknown C_c of the resonator and measure Q_{ext}. Therefore, the resonators were designed to have a low Q_{ext} in order to be able to measure it and being able to convert it into a value of the coupling capacitance without large errors.

Coupling regimes of a resonator

As mentioned, the amount of microwave photons that will leak out of the cavity resonator is govern by the coupling capacitor Q_{ext} and is therefore fixed. However, the amount that is leaking to the substrate and superconductor is governed by the temperature and will vary as the resonator is cooled down[2]. Thus, if only the design of the capacitor is within the correct order of magnitude, it will be possible to cross the point at which the $\mathrm{Q}_{ext} = \mathrm{Q}_{int}$. At this point the external losses equals the internal, the resonator is then *critically coupled* and from equation (2.10) it follows that

---

[2] Most of the losses at T $\geq$ 250 mK are due to quasi particle losses in the superconductor.

$$Q_{tot} = \left(\frac{2}{Q_{ext}}\right)^{-1} = \frac{Q_{ext}}{2} \tag{2.12}$$

Moreover, for the case when the internal losses dominate, *i.e.* $Q_{int} > Q_{ext}$, the resonator is *over-coupled* whereas when the external losses dominate, i.e. $Q_{ext} > Q_{int}$ it is *under-coupled.*

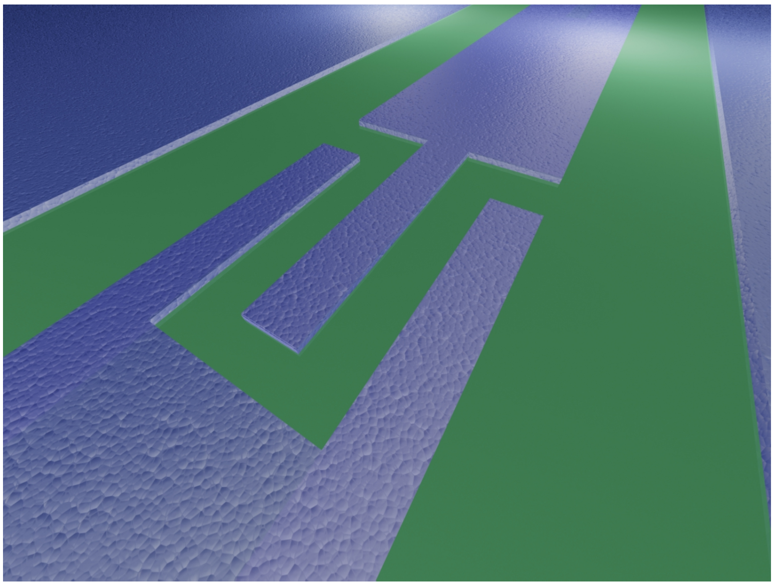

Figure 2.6: *The coupling capacitor is used to engineer the external Q-value of the resonator and thus its ability to store microwave photons.*

2.2.1 Transmons coupled to a tunable resonator

To be able to perform operations on the transmon, it needs to be connected to some "quantum bus". A novel solution was developed by Sandberg [23], based on a tunable cavity resonator, consisting of a $\lambda/4$ coplanar waveguide transmission line coupled to ground via a SQUID. By applying a magnetic field Φ_{ext} through the SQUID-loop placed in the end of the cavity, the resonance frequency of the cavity can be effectively tuned by changing its electrical length with a speed comparable to the speed of light. This transmission line can now play the role of a gate bias for a transmon once it is placed in the gap between the center strip of the cavity and ground, see Fig. 2.4 a). The transmon and the cavity are the focus of this thesis and can be described through the circuit diagram in Fig. 2.4 d).

Chapter 3

Modeling and designing the devices

The intention of this chapter is to outline the simulations that were done during the project to identify necessary design parameters as well as characteristic device parameters.

3.1 Simulations

Prior to any fabrication it is crucial to first model the devices. The starting point is to outline a framework of design constraints. These will later serve as guidelines for identifying remaining design parameters. This chapter is divided into three parts, ordered after appearance in the project.

The first part outlines a parameter framework that set the properties of the transmon. In this section, the anharmonicity of the transmon is investigated along with the interplay between its total capacitance, C_Σ and junction resistance R_N.

The second part describes the model used for designing the coplanar waveguide transmission line resonators.

The third part describes the model created for calculating the capacitance of an arbitrarily designed shunt capacitance of a transmon. For this experiment, only the shunt capacitance is considered and not the entire transmon.

3.1.1 Key parameters of the transmon

Anharmonicity

Since the transmon is intended to operate as an effective two-level system, the transition frequency between the ground state and the first excited state needs to be considered. The eigenenergy of the m^{th} energy level of the transmon can in the transmon regime be approximated as [5]

$$E_m \approx -E_J + \sqrt{8E_JE_C}\left(m+\frac{1}{2}\right) - \frac{E_C}{4}(2m^2+2m+1) \tag{3.1}$$

It is clear from the Fig. 2.3 that the charge dispersion of the transmon will be low enough to be robust to charge noise. However, for selective and fast control of the transmon, the anharmonicity needs to large enough, see Fig. 3.1. The relative anharmonicity is defined as

$$\alpha_r = \frac{E_{12}-E_{01}}{E_{01}}, \qquad E_{nm} = E_m - E_n \tag{3.2}$$

In Fig. 3.1, the relative anharmonicity is plotted as a function of E_J/E_C.

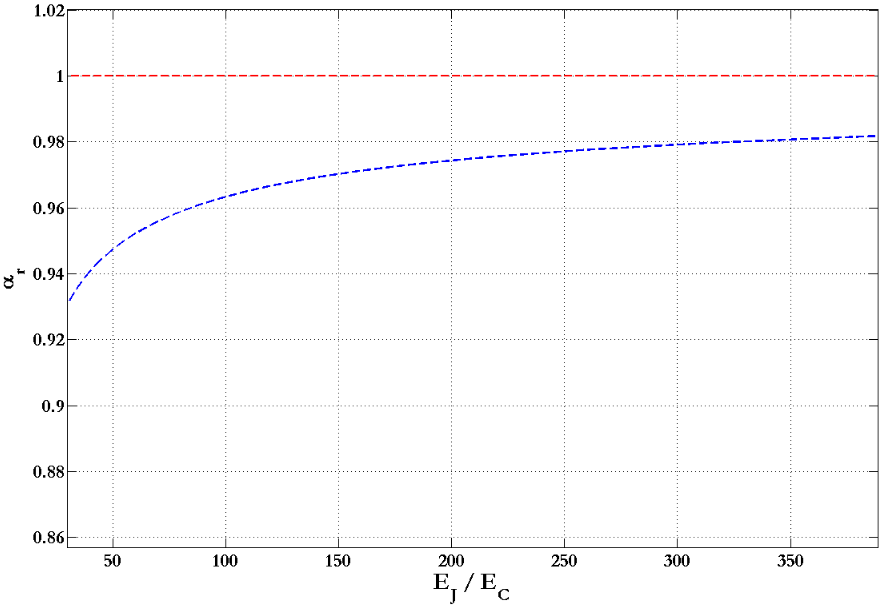

Figure 3.1: *The relative anharmonicity of the transmon as a function of E_J/E_C in the limit when $E_J/E_C \gg 1$. The curve approaches asymptotically unity as E_J/E_C goes to infinity. For the operating range of E_J/E_C presented, the anharmonicity is still well below one.*

Interplay between shunt capacitance and junction resistance

To investigate the parameter interplay of the transmon, a script was written in *Mathematica*, where an array of R_N values was used to calculate needed E_J/E_C for four different values of ν_p. The values of E_J/E_C were then used to also calculate the needed total capacitance C_Σ, see Tab. 3.1. In Fig. 3.2, E_J/E_C and C_Σ are plotted as functions of R_N. The transmon should be designed to stay within the two uttermost curves. Due to the fact that the two relevant design parameters of the transmon, R_N and C_Σ, are coupled in the ratio of $E_J \propto R_N^{-1}$ and $E_C \propto C_\Sigma^{-1}$, its possible to elaborate with the choice of parameters to obtain any required plasma frequency, ν_p[1]. Also, there could be situations when additional constraints are placed on one of the parameters. For instance, if one wants to minimize the length of the transmon, it will have a low C_Σ. This means that the junctions of the transmon must be smaller (or the oxidation pressure higher) in order to carry a large R_N.

ν_p[GHz]	5		5.25		5.75		6	
R_N[kΩ]	E_J/E_C	C_Σ[fF]	E_J/E_C	C_Σ[fF]	E_J/E_C	C_Σ[fF]	E_J/E_C	C_Σ[fF]
6.5	184.4	148.8	167.3	135.0	139.4	112.5	128.1	103.3
7.0	159.0	138.2	144.2	125.3	120.2	104.5	110.4	96.0
7.5	138.5	129.0	125.6	115.0	104.7	97.5	96.2	89.6
8.0	121.7	120.9	110.4	109.7	92.1	91.4	84.5	84.0
8.5	107.8	113.8	97.8	103.2	81.5	86.0	74.9	79.0
9.0	96.2	107.5	87.2	97.5	72.7	81.3	66.8	74.6
9.5	86.3	101.8	78.3	92.3	65.3	77.0	60.0	70.7
10.0	77.9	96.7	70.7	87.8	58.9	73.1	54.1	67.2
10.5	70.7	92.1	64.1	83.6	53.4	69.7	49.1	64.0
11.0	64.4	88.0	58.4	79.8	48.7	66.5	44.7	61.1
11.5	58.9	84.1	53.4	76.3	44.5	63.6	40.9	58.4
12.0	54.1	80.6	49.1	73.1	40.9	60.9	37.6	56.0
12.5	49.9	77.4	45.2	70.2	37.7	58.5	34.6	53.7
13.0	46.1	74.4	41.8	67.5	34.9	56.3	32.0	51.7
13.5	42.8	71.6	38.8	65.0	32.3	54.2	29.7	49.8
14.0	39.8	69.1	36.1	62.7	30.1	52.2	27.6	48.0

Table 3.1: *Shows a set of parameter combinations for the transmon qubit. The data has been calculated by first fixing R_N and ν_p, allowing to calculate the ratio E_J/E_C. Then, C_Σ was calculated from R_N and E_J/E_C.*

---

[1] $E_{01} \approx h\nu_p$, see equation (2.7).

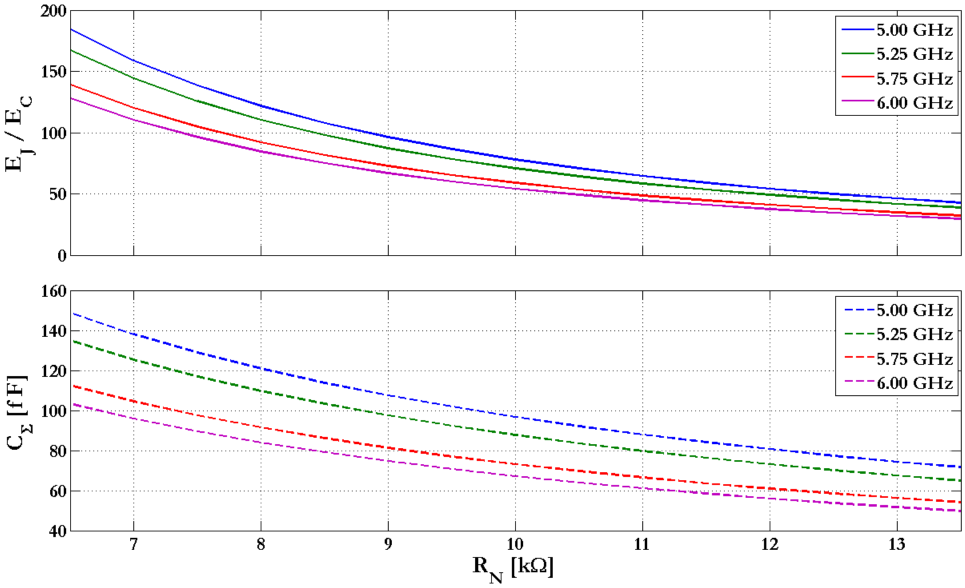

Figure 3.2: *The top plot shows the needed ratio of Josephson energy to charging energy* E_J/E_C *as a function of the normal state resistance* R_N *for the four different target frequencies* $\nu_p = 5.00, 5.25, 5.75, 6.00$ *GHz. In the same way the bottom plot shows the total transmon capacitance* C_Σ *as function of* R_N*.*

3.1.2 The transmission line

When designing a CPW it is essential to obtain an impedance match to the outside world. The waveguide should therefore have a characteristic impedance $Z_c = 50\ \Omega$. The characteristic impedance depends on the width of the center strip W and the gaps G, as well as the effective dielectric constant of the substrate. The transmons that are to fit inside the gaps of the CPW cavity have a width of 14 μm. Therefore, the gap width was set to G = 16 μm. A conformal mapping based model [25] was implemented in *Mathematica* to calculate Z_c as a function of the width of the center strip. The plot in Fig. 3.3 shows that the optimal width for obtaining Z_c = 50 Ω is W = 28 μm. In addition, the script calculates the capacitance per unit length, C_l, the inductance per unit length, L_l, and the effective dielectric constant, ε_{eff}[2]. Input for the model are the thicknesses and dielectric constants of the two layers of the substrate, presented in Tab. 3.2.

Layer	t [μm]	ε_r
SiO_2	0.4	3.9
Si	380	11.7

Table 3.2: *Shows the thicknesses, t and dielectric constants ε_r, from [26] of the two layers of the substrate.*

After the cross section dimensions have been identified, the length of the quarter wavelength resonator can be calculated from equation (2.8)

$$l = \frac{c}{4\sqrt{\varepsilon_{eff}} f_0} \tag{3.3}$$

where $f_0 = \frac{1}{2\pi\sqrt{L_l(C_r+C_c)}}$ is the resonance frequency of the cavity. In Tab. 3.3 all design parameters are listed.

G [μm]	W [μm]	ε_{eff}	C_l [pF/m]	L_l [μH/m]
16	28	6.66	172	0.43

Table 3.3: *Shows the simulated design parameters for the CPW with the substrate presented in Tab. 3.2.*

---

[2] This value was obtained from conformal mapping modeling but is too high. It should be lower.

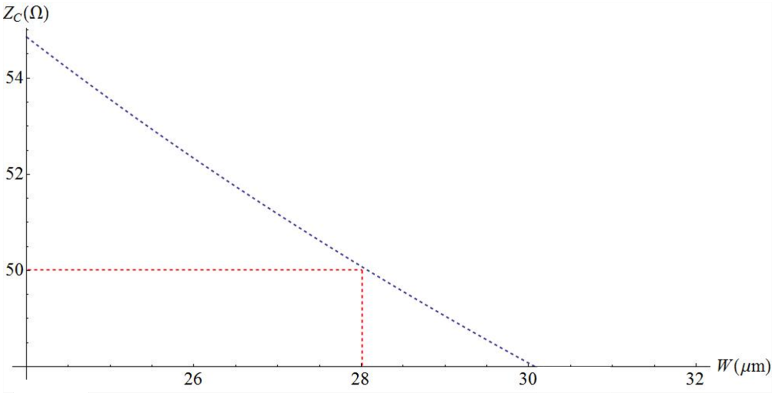

Figure 3.3: *The impedance of the CPW for a fixed gap width of 16 μm. To obtain a characteristic impedance of $Z_c = 50\ \Omega$, the center strip should be designed to have a width of $W = 28\ \mu m$.*

3.1.3 Model for the shunt capacitance of the transmon

The total capacitance of the transmon can be written as the sum of three contributions, recall Fig. 2.4

$$C_\Sigma = C_s + C_g + C_J \tag{3.4}$$

One of the cornerstones of this thesis is to investigate the largest of these contributions *i.e.* the shunt capacitance, C_s. For this reason, another script was written, based on a paper from Gevorgian *et al.* [27]. The model uses conformal mapping for simulating the capacitance of interdigital finger capacitors, see Fig. 3.4. A general design constraint was to fix the width of the transmon to 14 μm. Thus, the parameters of the interdigitated capacitance as defined in Fig. 3.5 has to satisfy $2w + 2g_{end} + l = 14\ \mu\text{m}$.

Variation of ratio of finger- and gap width

A way of optimizing the transmon would be to make it as short as possible, maintaining a sufficient high shunt capacitance. An obvious way to obtain a high shunt capacitance is to increase the number of fingers, N on the two islands. However, more interesting is to investigate how to optimize C_s for a fixed length of the transmon, $L = N(s+g) = constant$. The effect on the shunt capacitance is investigated by varying the ratio $\frac{s}{g}$. The results from this simulation are presented in Tab. 3.4 and plotted in Fig. 3.5 a).

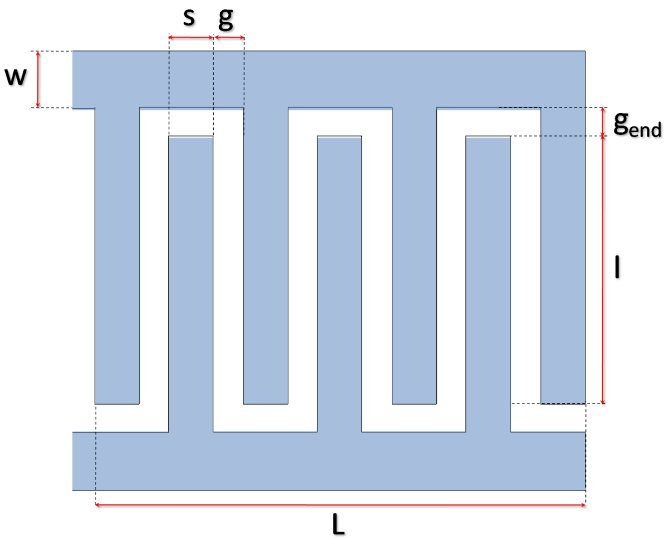

Figure 3.4: *The design dimensions used as model input in the interdigital finger capacitor model.*

Variation of the finger width

Another way of increasing the shunt capacitance would be to shrink the finger width s, to have place for a larger number of fingers. For this simulation, the transmon length was fixed along with the gap width to $L = 200$ μm and $g = 0.3$ μm, respectively. Due to the finite thickness of the aluminum films, an effective finger width s_{eff} was calculated resulting in slightly wider fingers than the designed width. However, this simulation indicated no big improvement of the shunt capacitance. The results are presented in Tab. 3.5 and plotted in Fig. 3.5 b).

The purpose of writing this script is twofold; the first is to find a starting guess of the shunt capacitance of the transmon to ensure that the capacitance will give an external quality factor within a measurable range, the second is to generate better values after being calibrated from the first measurements.

s[μm]	g[μm]	s/g	C$_s$[fF]	C$_s$/C$_s$(s=g=1)
1.0	1.0	1.00	63.5	1.000
1.1	0.9	1.22	67.1	1.057
1.2	0.8	1.50	70.4	1.108
1.3	0.7	1.86	73.3	1.153
1.4	0.6	2.33	75.6	1.190
1.5	0.5	3.00	77.1	1.215
1.6	0.4	4.00	77.6	1.222
1.7	0.3	5.66	76.5	1.204
1.8	0.2	9.00	72.4	1.140

Table 3.4: *The results from simulating shunt capacitances of fixed length $L = 100\ \mu m$ and sum of finger and gap width $s + g = 2\ \mu m$. The simulation shows that a maximum increase (22%) of C_s is obtained for the ratio $s/g \approx 4$.*

3.2 Sample layouts

Two main sample structures were used in the project. First, for comparing different Josephson junction designs, these should be fabricated on the same chip to undergo the same treatment. To accomplish this, arrays of test structures were fabricated, see Fig. 3.6. Second, the resonator cavities were fabricated for the investigation of the coupling capacitors and shunt capacitances, see Fig. 3.7.

s[μm]	n	C$_s$[fF]	C$_s$/C$_s$(s=g=0.5)
0.5	200	75.93	1.000
0.6	182	77.15	1.016
0.7	167	77.95	1.027
0.8	154	78.28	1.031
0.9	143	78.47	1.034
1.0	133	78.21	1.030
1.1	125	78.30	1.031
1.2	118	78.33	1.032
1.3	111	77.74	1.024
1.4	105	77.30	1.018
1.5	100	77.14	1.016

Table 3.5: *The results from simulating shunt capacitances of fixed length $L = 100$ μm and gap $g = 0.5$ μm and varying the finger width. The simulation indicate that this variation has negligible effect on C_s by only increasing it with a few percent.*

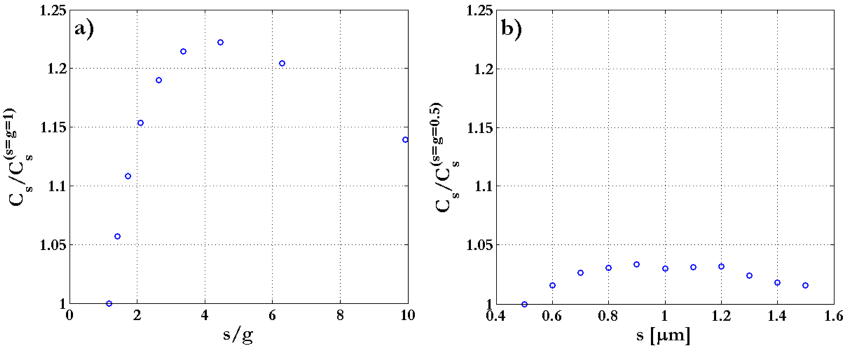

Figure 3.5: ***a)*** *the effect on the shunt capacitance of varying the width ratio between finger and gap. The model indicate a maximal increase of 22% for $s/g = 4$.* ***b)*** *results from simulating shunt capacitances of fixed length $L = 100$ μm and gap $g = 0.5$ μm and varying the finger width are presented. These simulations indicate that this variation has negligible effect on C_s by only increasing it with a few percent.*

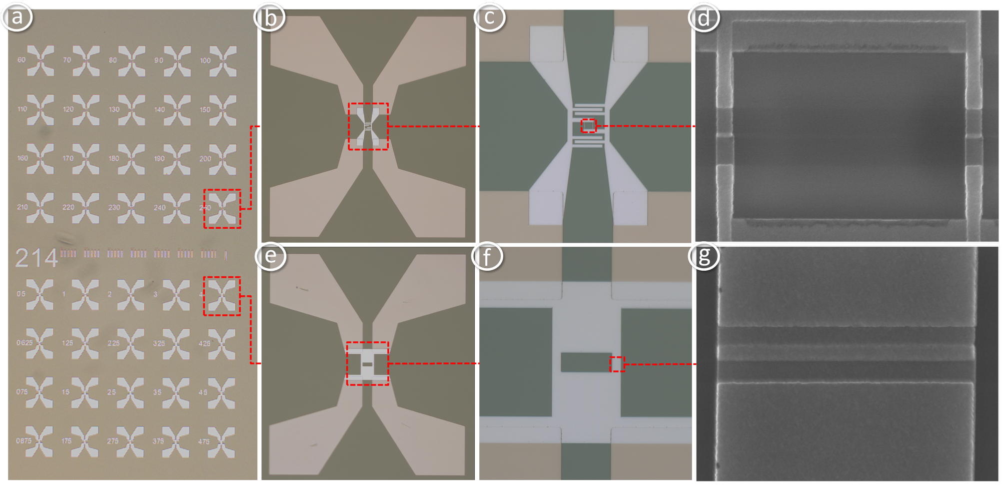

Figure 3.6: ***a)*** *Micrograph of one of the test structure chips used to measure transmon and cavity tuning SQUIDs.****b)*** *and* ***c)*** *Transmon test structure connected to gold pads.* ***d)*** *A SEM image of the two tunnel junctions.* ***e)*** *and* ***f)*** *Cavity tuning SQUID connected to gold pads.* ***g)*** *A SEM image showing one of the two junctions.*

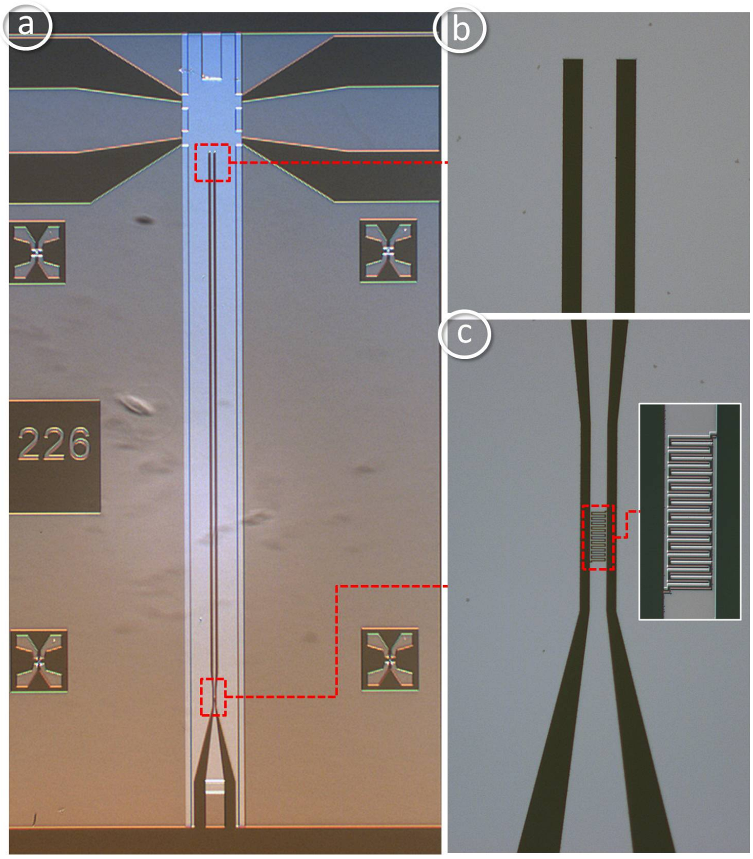

Figure 3.7: ***a)*** *Micrograph of a resonator chip used to measure the shunt capacitance of the transmon.* ***b)*** *The shorted end of the CPW gives a* $\lambda/4$ *resonator.* ***c)*** *the coupling capacitance has the shape of the shunt capacitance of the transmon. The only variable is the number of fingers.*

Chapter 4

Experiments

The intention of this section is to introduce the techniques used to fabricate cavities and transmons as well as the experimental setup used to measure the devices.

4.1 Sample fabrication

A crucial condition when fabricating devices containing features on the nanoscale is that it is carried out within a clean and well controlled environment. All fabrication throughout this thesis project has been done in the Nanofabrication Laboratory at Chalmers University of Technology. All devices were fabricated on standard three inch silicon wafers. A layer of 400 nm wet oxide was grown on the wafers prior to fabrication. Throughout this section, the most essential process considerations are presented. For a detailed recipe, see appendix [A].

4.1.1 Photolithography

Since the features of the devices range from large structures of several millimeters down to narrow tunnel junctions of the order of hundred nanometers, two different lithography techniques are used. First, all large features, including contact pads and ground planes, are patterned using photolithography. This is done by first spinning two layers of resist; one *lift-off resist* and one *photoresist*. The type of photoresist used was a positive one which consists of polymer chains that will break when exposed to UV light and easily dissolved in a developer. To cover the parts of the wafer which should not be exposed a mask is used. The bottom layer of resist has the property of dissolving in all directions from where it is reached by the developer. This will result in so called undercut reaching underneath parts of the photoresist. Obtaining decent undercut is crucial for a successful lift-off process of the excess material after deposition, see Fig. 4.1.

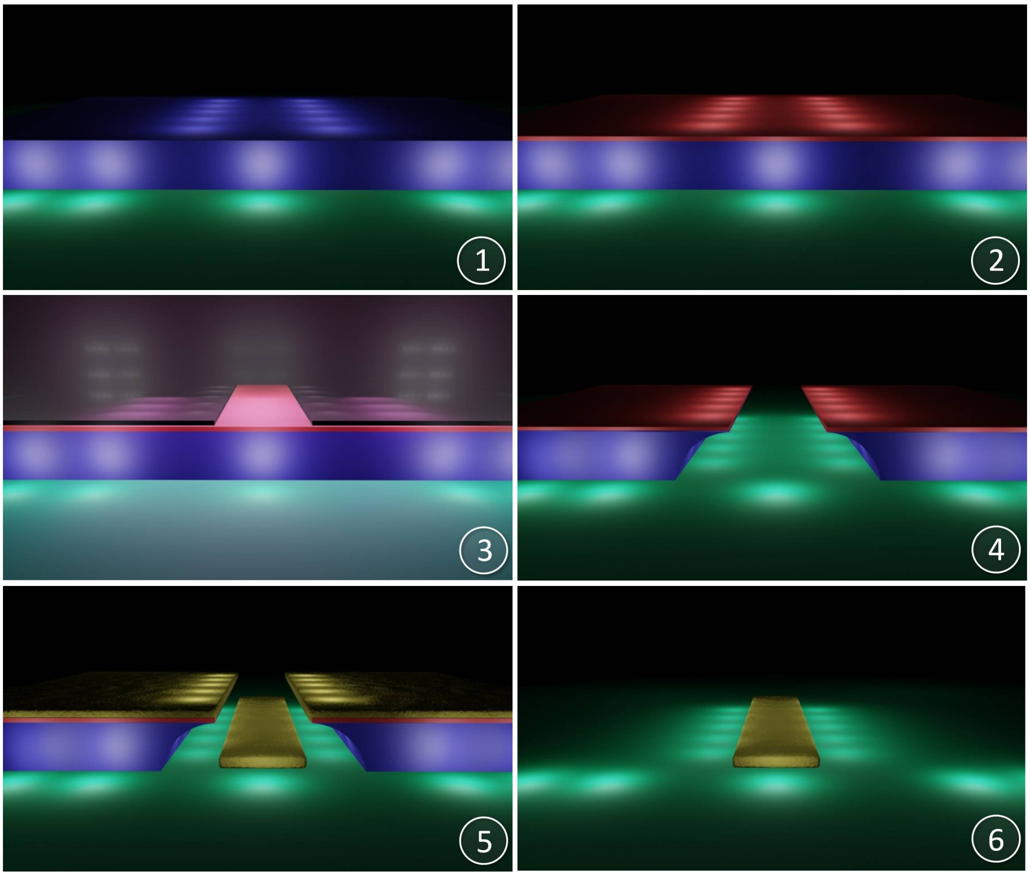

Figure 4.1: *Shows a sequential description of the photolithography process.* ***1)*** *The wafer is coated with a lift-off resist and soft baked.* ***2)*** *Positive photoresist is spun on top of the lift-off layer and soft baked.* ***3)*** *A chromium mask is used to define the pattern. Once the mask has been aligned, the mask is exposed to UV-light.* ***4)*** *Developing the two resists will create undercuts and leave the masked parts of the photoresist. The remaining resist cover the parts where metal is undesired.* ***5)*** *A thin film of metal is deposited. Due to the undercuts, there is no step-coverage to the metal on top of the resist.* ***6)*** *Finally, in a lift-off step, the excess metal is removed by dissolving its supporting resist layers leaving only the desired metal.*

4.1.2 Electron beam lithography

Due to the limited resolution of photolithography, another lithography method is needed to define features that are smaller than a couple of microns. The method used is called electron beam lithography and utilizes, as the name reveals, a beam of electrons to expose any desired area on the wafer. As oppose to the photolithography there is no need to first fabricate a mask. Instead, the pattern is drawn in *AutoCAD*. In principle, all structures could be written by using electron beam lithography. However, as this method requires a far more expensive machine and also takes hours instead of minutes, it is preferable to save it for the very small features without compromising the final quality of the device. However, when designing devices including a lot of corners and turns *i.e.* a transmon qubit, a substantial amount of unwanted *proximity effect* will come into play and expose undesired parts of the substrate. This effect is a consequence of electrons that undergoes random backscattering after passing through the resist, thus exposing a larger area than intended. To compensate for this effect, a *proximity correction* is done which means that the layer in the CAD file is divided into 16 new layers with different assigned doses that will even out the dose of exposure throughout the design.

4.1.3 Two-angle evaporation

After defining the smallest features in the electron beam lithography, all Josephson junctions can be created by using two-angle evaporation (shadow evaporation) of aluminum[1]. A sequential description of this process is shown in Fig. 4.2. The outcome of this technique is heavily dependent upon the thicknesses of e-beam resist and lift-off layer. To create a Josephson junction, all lift-off resist underneath the junction region must be removed, creating a bridge of e-beam resist. Due to the small dimension of the junctions it is hard to investigate the undercuts prior evaporation using an optical microscope. Instead, the two-angle evaporation should be carried out before the undercut can be properly investigated. Fortunately, since the tunnel barrier has a normal state resistance, R_N, a signature of its physical size can be collected by measuring its resistance using a four-probe setup described in section [4.2.2].

The first step of the evaporation process is to deposit a layer of Al, having the sample tilted an angle α. Then, the thin tunnel barriers of AlO_x are formed by letting oxygen gas of controlled pressure, P_{ox} pass into the evaporation chamber. After a desired oxidation time, t_{ox} the oxygen gas is pumped out of the chamber and a second layer of Al is evaporated from an angle of $-\alpha$. If all resist has been removed underneath the bridge, an overlap of Al will arise between which the

---

[1] This technique is also known as the "Dolan technique" after the inventor GJ Dolan.

tunnel barrier is formed. Important is to make the second layer thicker than the first one to achieve a sufficient step coverage. By elaborating with the junction design, any desired dimension of the tunnel barrier area can be achieved down to 30×30 nm^2. Another way to affect the resistance of the tunnel barrier is to change the thickness of the oxide layer, governed by the two oxidation parameters t_{ox} and P_{ox}. However, it is important to take into consideration that all features of the sample will undergo the same two-angle evaporation process. Therefore, all regions of the sample need to be designed to match after the process.

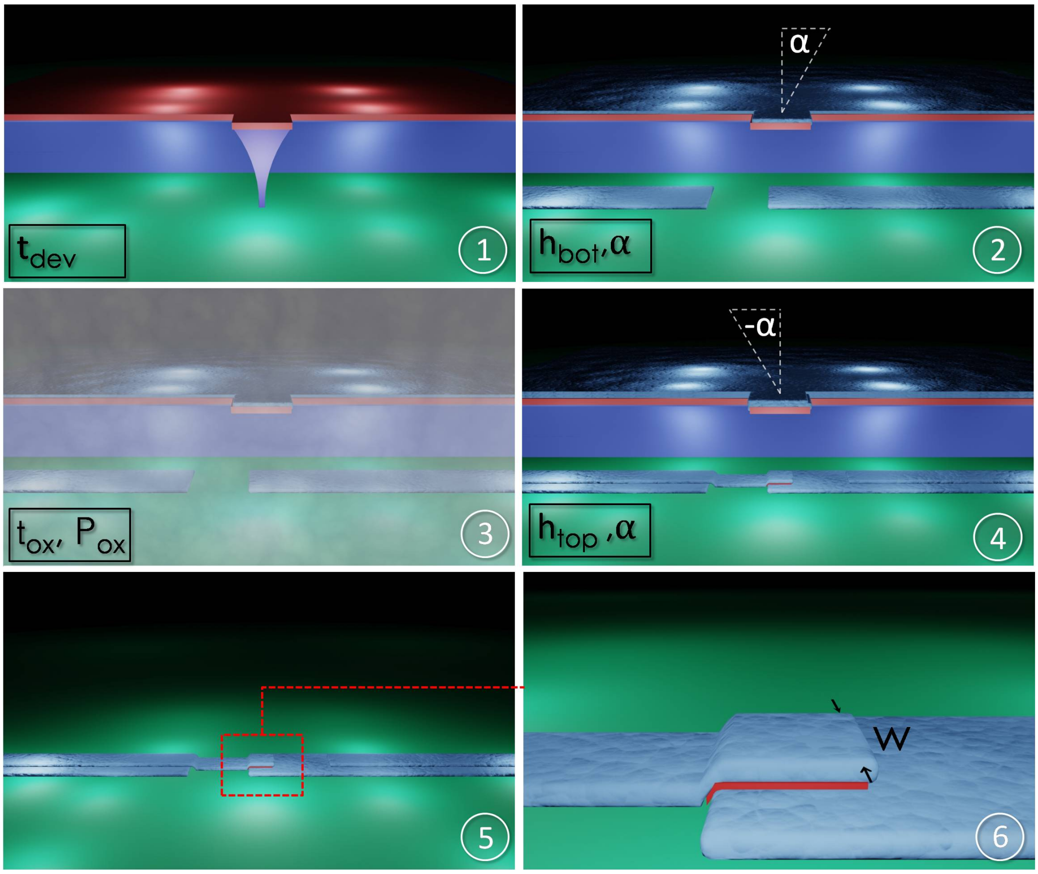

Figure 4.2: *A sequential description of the two-angle evaporation process to form a Josephson junction. The controllable parameters in each step are shown in the black boxes.* ***1)*** *A narrow part of the resist is defined by the e-beam lithography. The bottom resist is developed for a long enough time,* t_{dev} *to form a suspended bridge of top resist.* ***2)*** *The first layer of Al is evaporated from an angle* α*. The height of the bottom electrode is denoted* h_{bot}*.* ***3)*** *Oxygen gas of pressure* P_{ox} *is let into the chamber to form a very thin oxide on top of the aluminum. The oxide thickness is governed by the oxidation time,* t_{ox}*.* ***4)*** *A second layer of Al is evaporated from an angle of* $-\alpha$*. The height of the top electrode is denoted* h_{top}*.* ***5)*** *The Josephson junction is now created in the small region where the two layers overlap each other.* ***6)*** *The AutoCAD design used in the e-beam will define the junction width,* w*.*

The Plassys evaporator

The "Plassys" is a computer-controlled evaporator dedicated for depositing aluminum, see Fig. 4.3. It is able to tilt the sample holder with high precision, which makes it suitable for two-angle evaporation. In addition, there is two different processes for oxidation, namely dynamic and static. During dynamic oxidation, the oxygen gas is continuously exchanged and the pressure is controlled through a PID regulator capable of oxygen pressures up to 0.3 mbar. For static oxidation, oxygen gas is let into the chamber to stay there throughout the desired oxidation time. When using static oxidation, higher pressures can be used. A tunnel junction guide for the Plassys is provided in Appendix [B].

The sample is mounted in a load-lock, separated from the source chamber by a gate valve. This leads to fairly short pump-down times. To reach a base pressure of $3 \cdot 10^{-7}$ mbar takes approximately $1\frac{1}{2}$ hours if the sample chamber has been vented for a short time[2].

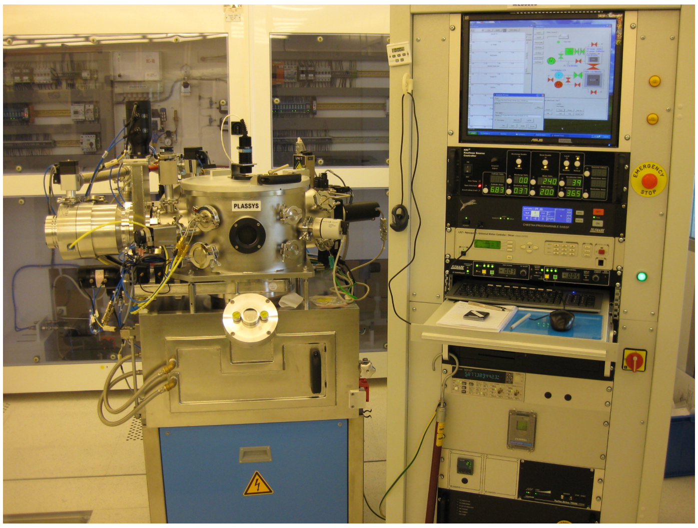

Figure 4.3: *Shows the front side of the Plassys evaporator. The evaporator is fully controlled by the computer interface to the right.*

---

[2] The required pump time is highly dependent on how long time that has passed with the chamber vented.

4.2 Measurement setup

4.2.1 Cryogenics

In order to investigate the Q_{ext} of resonators, measurements at temperatures well below the critical temperature at which Al becomes superconducting were needed. However, since no real qubits were measured it was sufficient that the resonators passed through the critical coupling point. Thus, it is unnecessary to use dilution refrigerators which typically take several days to cool down and has a substantially higher cost of operation. Instead, a ^{3}He-based cryostat was used throughout the measurements.

Microwave reflection setup in the HelioxVL cryostat

The Oxford Instruments HelioxVL system is a ^{3}He charcoal-absorber based cryostat with a base temperature of 270 mK. For information about the operational principles of the cryostat, see [28]. In Fig. 4.4, a schematic illustration of the cryostat wiring is presented. The first port of a vector network analyzer is connected to a directional coupler with 30 dB coupling and 20 dB directivity. The microwave signal then passes through a band pass filter and a couple of attenuators before it is reflected in the resonator, which is mounted at the coldest part of the cryostat. The reflected signal goes through the directional coupler and up to the second port of the vector network analyzer. Thus, the reflection measurement looks like a transmission from one port to the other.

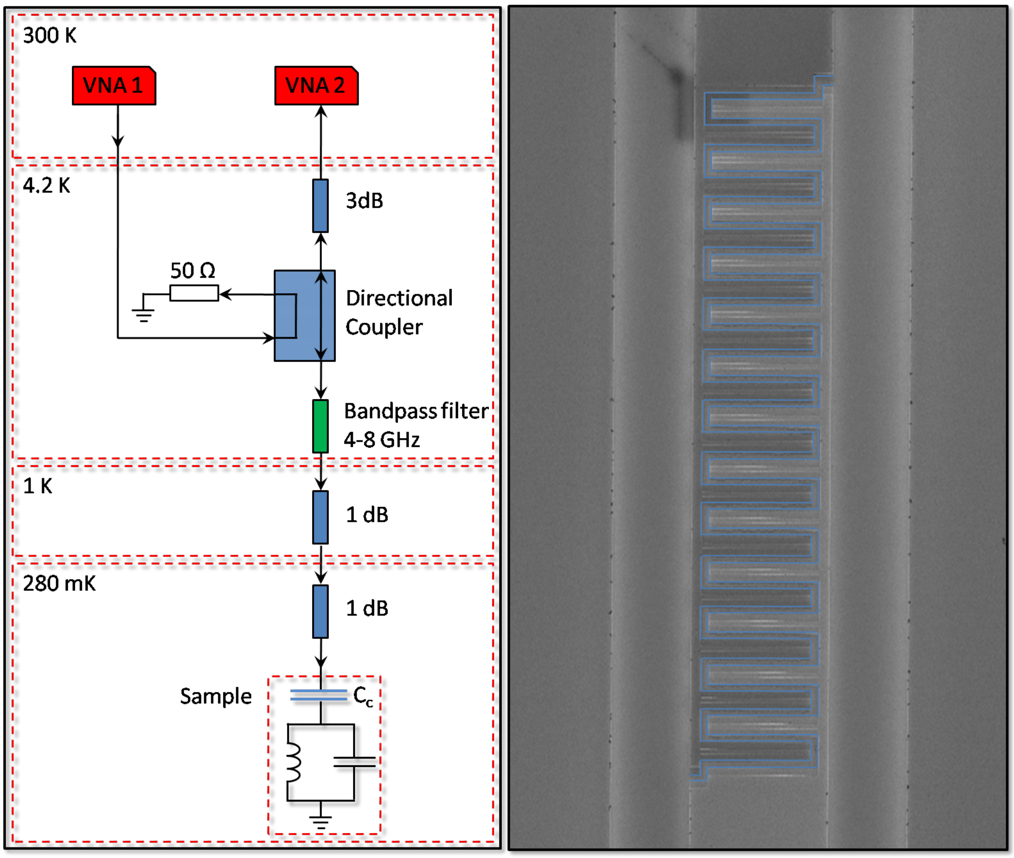

Figure 4.4: *Schematics of the microwave wiring used during the shunt capacitance experiment. VNA 1, the first port of a vector network analyzer, is connected to a directional coupler. The directional coupler has a coupling of 30 dB and a directivity of 20 dB. The microwave signal continues through a band pass filter and a couple of 1 dB attenuators before it reaches the coldest part of the system where the resonator is mounted. The attenuators are used to thermally anchor the coaxial cable at the 1K-pot. The signal gets reflected in the resonator and goes back up through the directional coupler, which prohibits the signal from VNA 1 to contribute to the outgoing signal. The signal is finally detected in port VNA 2. A power of -20 dBm was used.*

4.2.2 Normal state resistance measurements

By measuring the normal state resistance, R_N of the fabricated Josephson junctions, a signature of its physical size can be obtained. However, due to the native oxide on top of the Al film in combination with the small features of the device, the junctions positioned inside the device are difficult to probe. Instead, test structures of identically designed junctions, connected to gold pads, were added on the chips. To get as representative measurement as possible, a four-probe setup was used in a parameter analyzer (subtracting intrinsic resistance of the circuitry), see Fig. 4.5.

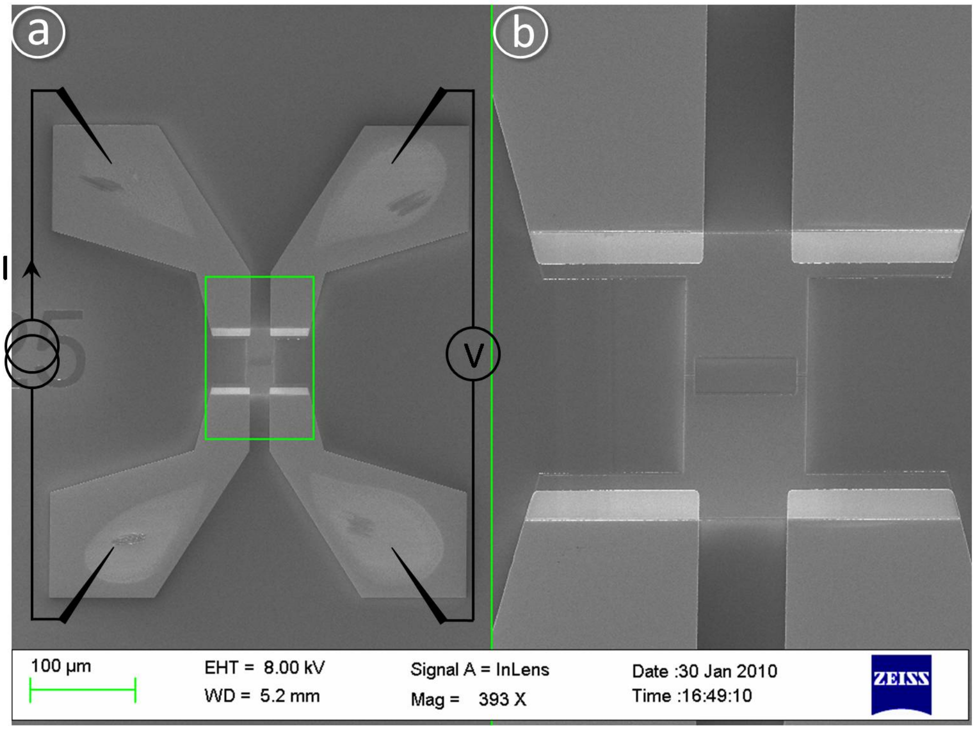

Figure 4.5: *The measurement setup of the parameter analyzer described in a SEM image of a SQUID test structure.* ***a)*** *A current is applied between the two gold pads on the left-hand side, while the voltage over the junctions is measured between the two gold pads on the right hand side. By measuring the voltage for a sweep in current, the resistance can be extracted through Ohm's law. The advantage of using a four-probe setup over a two-probe one is the ability to subtract the intrinsic resistance of the circuitry.* ***b)*** *A zoomed in image of the SQUID, connected to the four gold pads.*

Chapter 5

Results and discussion

The intention of this chapter is to outline the main findings of the diploma work, along with some remarks about the way of proceeding.

5.1 Shunt capacitance experiment

The sizes of the shunt capacitors were extracted by measuring the external Q-value of resonators coupled to the environment through identical interdigital finger capacitors as used for transmon shunt capacitances. The resonance frequency of each resonator was detected by sweeping the probe signal over an interval in frequency and observe the magnitude and phase responses of the reflection coefficient, S_{11}. A background trace was taken upon cooling just before the signal started to indicate signs of change in magnitude and phase. During the cooling down sequence below the critical temperature of the Al, the Q_{int} of the resonators will increase (as oppose to Q_{ext} which is fixed by the geometry). This is due to the decreased number of quasi particles. Thus, a shift in the relation between Q_{int} and Q_{ext} will take place and for a certain temperature - the resonator will be critically coupled. The magnitude and phase of S_{11} for the transition between under- and over-coupled for one of the resonators are plotted in Fig. 5.1. To be able to measure at critical coupling, the electrical delay of the VNA was tuned in to compensate for the length of the cables. Then, by slowly heating the resonator through critical coupling, a trace was taken at the point when the 360° phase wrap occurred in the phase response.

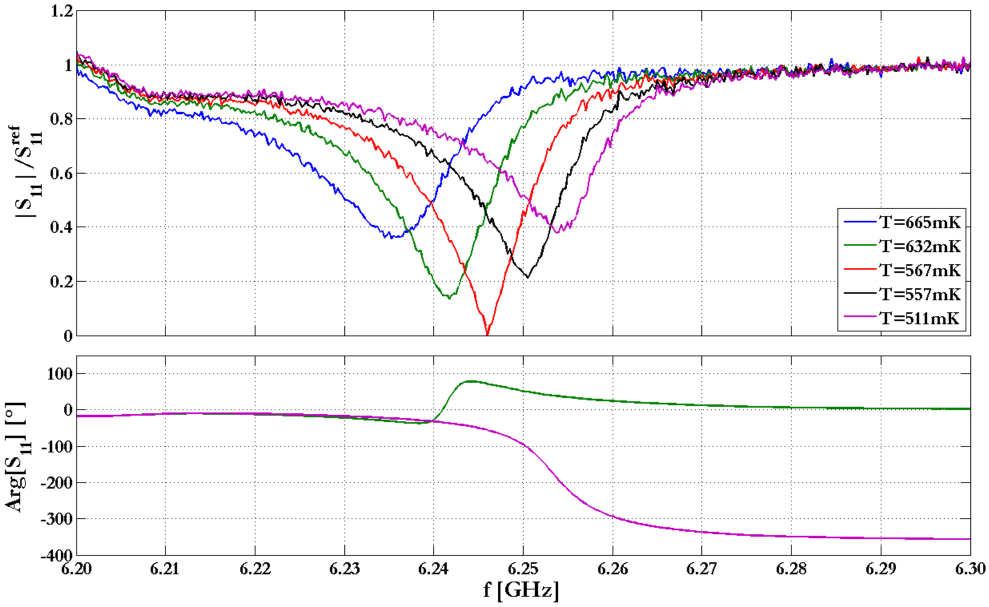

Figure 5.1: *The magnitude (top) and phase (bottom) of the reflection coefficient (S_{11}) for a resonator with a 10 finger coupling capacitor. The five trace sequence of the magnitude is taken for different sample temperatures during cool down. Critical coupling was found at 567 mK (red curve). At this temperature, no signal gets reflected, resulting in a V-shaped peak. For T>567 mK, the resonator is under-coupled while for T<567 mK it is over-coupled. For the phase response, this transition sequence results in a 360° phase wrap.*

Extraction of external quality factor

The Q$_{ext}$ can be extracted by using equations (2.10) and (2.12).

$$Q_{tot} = \frac{f_0}{\delta f} = \frac{Q_{ext}}{2} \tag{5.1}$$

where f_0 is the resonance frequency of the resonator and δf represents the width of the peak, see Fig. 5.2. However, since the peak is no longer Lorentzian shaped at critical coupling, δf can not be interpreted as Full Width Half Maximum (that would be the case for a Lorentzian peak). Instead, to investigate the correct reflection coefficient at which the values should be extracted, the width needs to be taken at another point in reflection coefficient. To investigate where, consider the expression for the reflection coefficient of a parallel LCR resonator[24]

$$S_{11} = \frac{Z_L - Z_0}{Z_L + Z_0} = \frac{1 - \omega^2 L(C + C_c(1 - \frac{Z_0}{R})) + j\omega(\frac{L}{R} - Z_0 C_c(1 - \omega^2 LC))}{1 - \omega^2 L(C + C_c(1 + \frac{Z_0}{R})) + j\omega(\frac{L}{R} + Z_0 C_c(1 - \omega^2 LC))} \tag{5.2}$$

Now, by first assuming that the internal resistance of the resonator is much larger than the load resistance (50 Ω), equation (5.2) can be simplified to

$$S_{11} = \frac{1 - x^2 + jx\left(\frac{1}{Q_{int}} - \frac{1}{Q_{ext}}\frac{1-kx^2}{1-k}\right)}{1 - x^2 + jx\left(\frac{1}{Q_{int}} + \frac{1}{Q_{ext}}\frac{1-kx^2}{1-k}\right)} \tag{5.3}$$

where $x = \frac{\omega}{\omega_0}$, $k = \frac{C}{C+C_c}$ and the quality factors are expressed as $Q_{int} = \omega_0 R(C + C_c)$ and $Q_{ext} = \frac{C+C_c}{Z_0 C_c^2 \omega_0}$. By further assuming that $\omega_0 Z_0 C \ll 1$ and $Q_{ext} \gg 1$ the following is obtained

$$S_{11}|_{x=1+\frac{1}{2Q_{tot}}} \rightarrow \frac{1}{\sqrt{2}} \tag{5.4}$$

Thus, instead of taking the δf at $\frac{1}{2}$, it should be extracted at $\frac{1}{\sqrt{2}} \approx 0.707$ of the maximum reflection coefficient. This was done using the two plateaus to the left and right of the resonance frequency f_0 as boundaries within which the correct value should lie, see Fig. 5.2. From the measured values of Q$_{ext}$, the coupling capacitances were calculated using equation (2.11). The extracted coupling capacitances are plotted in Fig. 5.3. In addition, the modeled values of the shunt capacitance are plotted as a comparison. All extracted parameters for the resonators are presented in Tab. 5.1.

From Fig 5.3 it can be concluded that the measured data has a stray capacitance even for zero fingers. This is due to the gap that would remain in the capacitor and the long-range capacitance between the center strip of the CPW and the incoming

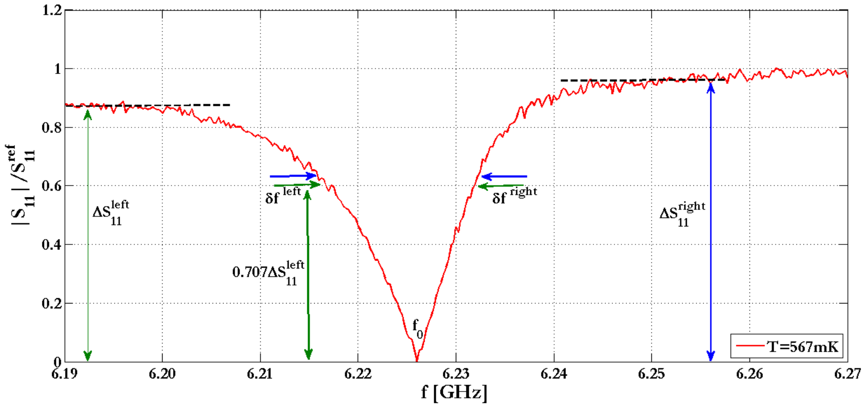

Figure 5.2: *To localize the peak width in the magnitude plot for the critically coupled resonator, two plateaus with heights* ΔS_{11}^{min} *and* ΔS_{11}^{max} *were chosen as boundaries. From these,* δf^{min} *and* δf^{max} *were calculated.*

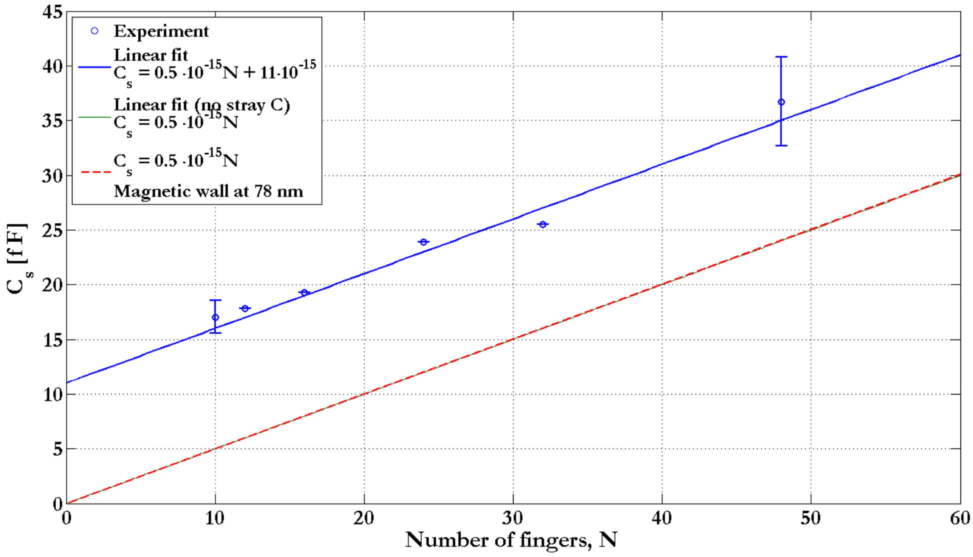

Figure 5.3: *The extracted coupling capacitances from measuring the* Q_{ext} *of resonators having capacitors with different number of fingers compared with the model (red).*

N	f_0 [GHz]	$\delta f^{min}, \delta f^{max}$ [MHz]	Q_{ext}^{min}, Q_{ext}^{max}	C_s^{min}, C_s^{max} [fF]
10	6.246	16, 19	657, 781	16.29, 17.80
12	6.232	19, 19	656, 656	17.83, 17.83
16	6.213	22, 22	565, 565	19.28, 19.28
24	6.169	33, 33	374, 374	23.92, 23.92
32	6.140	38, 38	323, 323	25.48, 25.48
48	5.968	63, 78	153, 189	34.69, 38.77

Table 5.1: *Shows the extracted parameters from the Heliox cryostat measurements of the external Q-values for transmon shunt capacitors with different number of interdigital fingers, N. Some of the measured resonance peaks were asymmetric, resulting in an interval for δf and thus also for Q_{ext} and C_s.*

transmission line. The capacitance per finger is 0.5 fF and the long-range offset for the CPW (W = 28 μm, G = 16 μm) is 11 fF. However, since this effect will only occur when the capacitor is placed as a coupling capacitor and not inside the gap of the CPW, it is subtracted from the line. The resulting line through zero was then fitted using the magnetic wall[1] as the only fitting parameter. For a magnetic wall x = 78 nm, an agreement between the fit and the model was found.

---

[1] The magnetic wall is a symmetry line used in the model [27].

5.2 Normal state resistance experiment

The investigated tunnel junctions can be divided in two categories after their size; larger tunable cavity SQUID junctions and smaller transmon junctions.

5.2.1 Tunable cavity SQUIDs

First, in order to get familiar with the interplay between the parameters of the oxidation process and the obtained junction resistance R_N, tunable cavity junctions with substantially larger junction area than the transmons were initially investigated. The obtained values can later serve as guidelines in the design of tunable resonators as well as SQUIDs for other devices.

Dependence on oxidation pressure and time

By fixing the evaporation angles, the impacts of the oxidation time t_{ox} and pressure P_{ox} was investigated. A fairly long oxidation time of $t_{ox} = 30$ min was chosen to minimize the effect of varying bleed rate *i.e.* the flow rate of oxygen into the chamber during oxidation of the junctions. The oxidation is a diffusive process and the thickness of the oxide has a logarithmic increase over time. To check that this "slow limit" is reached, two oxidations where done using the same pressure, but varying the t_{ox}. The results indicate that this change of t_{ox} has very small effect upon the junction resistance and thus the oxide. However, by instead changing the oxidation pressure P_{ox}, a large effect on the junction resistance was obtained. The measured resistances are plotted in Fig. 5.4 a) and the corresponding conductance $G = R_N^{-1}$ in Fig. 5.4 b) where each curve represent one chip. In the design, the width of the junctions was varied whereas the overlap was fixed on each chip. The results from these chips are summarized in Tab. 5.2. A design guide for SQUIDs is provided in Appendix [B].

Note that the conductance plot shows that the points at large area generally have a larger deviation from the fitted function than the points at smaller area. This seems counter-intuitive as one would expect large junctions to be more predictable. However, the reason for this deviation is not the uncertainty of the junction size but rather the low resistance of the large junctions. The deviation from the curve is an effect of settings of the parameter analyzer rather than area deviations.This can be concluded by noting that the large junctions for the red curve with the higher oxidation pressure do not show this behavior.

Another important feature of this data is the two regions of junction areas. For small junction areas, deviations from the designed area leads to relatively large deviations in resistance whereas large junction areas are less sensitive to such deviations. As mentioned before, these deviations are not present for this large junctions but will play a key role in the fabrication of junctions inside of transmons when the area of the junctions is of the same order of magnitude as the grain size of the aluminum.

P_{ox} [mbar]	t_{ox} [min]	ρ $[\Omega/\mu m^2]$	$\sigma[\mu m^2/\Omega]$
0.2	30.0	121.9±4.1	$8.455 \cdot 10^{-3} \pm 3.6 \cdot 10^{-4}$
0.2	27.5	125.7±2.1	$7.963 \cdot 10^{-3} \pm 2.2 \cdot 10^{-4}$
1.0	30.0	477.7±3.8	$2.138 \cdot 10^{-3} \pm 0.4 \cdot 10^{-4}$

Table 5.2: *A summary of the results from the three samples evaporated in the Hobbykit. Resistivity and conductance are extracted from the fits in Fig. 5.4*

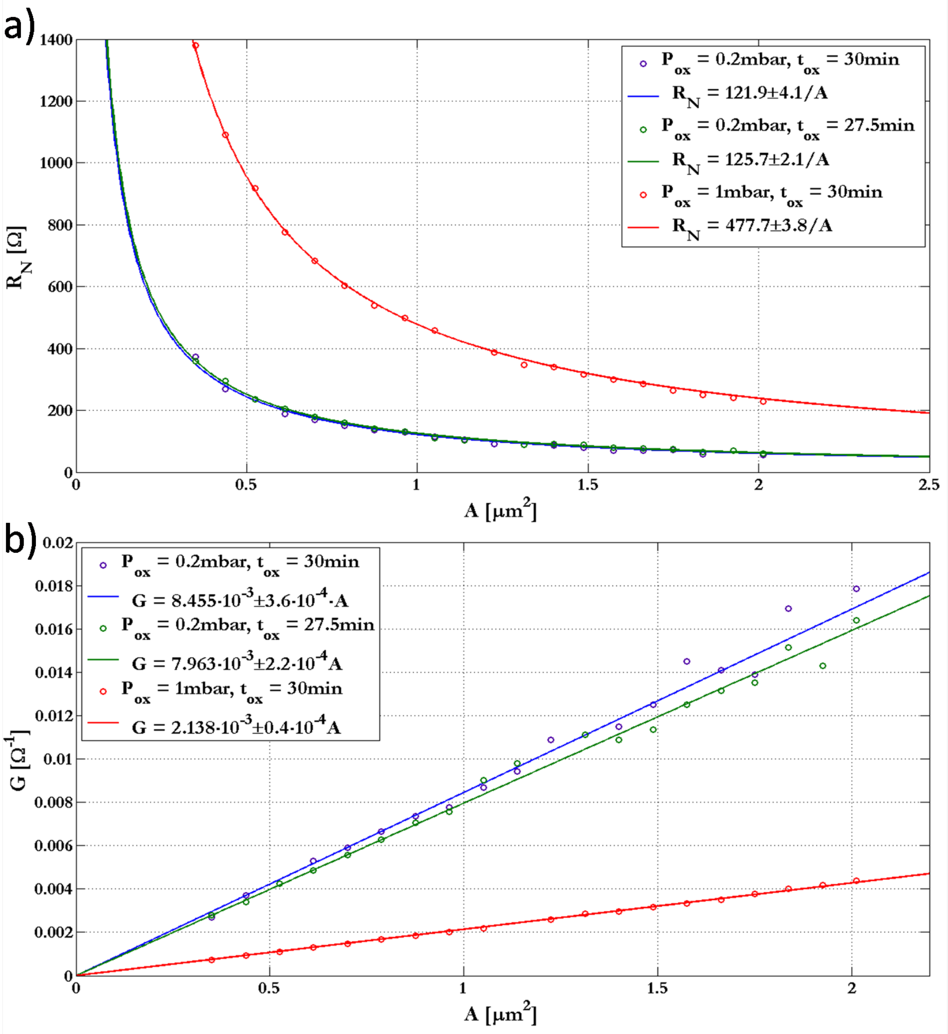

Figure 5.4: ***a)*** *The resistance as function of the junction area for three samples evaporated in the "Hobbykit". The plot clearly illustrate the impact on R_N of varying the evaporation pressure in the the two-angle evaporation process.* ***b)*** *The corresponding conductance $G = R_N^{-1} = \sigma A$ of the measured R_N values.*

5.2.2 Transmon junctions

The starting point of the fabrication of transmon junctions was a designed area of $\approx 100 \times 100$ nm^2. However, these small junctions turned out to be difficult to reproduce. One of the motivations for the small dimensions was to obtain a large junction resistance of the order of $R_N \approx$7 kΩ. However, as illustrated for the large tunable cavity junctions this could also be done by increasing P_{ox} and fabricate slightly larger junctions. On each chip, the area was varied both through the overlap and the width of the junctions. The red and the blue curves correspond to two chips whereas the rest are one chip each. In Fig. 5.5 a) the junction resistances are plotted as function of the junction area. The corresponding conductances are plotted in Fig. 5.5 b).

Reproducibility of transmon junctions

When fabricating transmons coupled to the cavity, it is not convenient to measure the R_N of the junctions inside of the device. Instead, test structures like the ones measured here are placed on the edges of each chip having the same design as the junctions inside the device. For this reason, to engineer a reproducible system it is sufficient if these test structures provide a signature of the junctions inside the device. From the conductance plot in Fig. 5.5 b), a quantitative reproducibility analysis can be done by calculating the deviation of each data point from the fitted function, $\Delta G(A_i)/G(A_i)$. The result is presented in form of a histogram of the 110 junctions in Fig. 5.6 a). The distribution is well centered around zero, indicating a good agreement of the fitted linear functions. The standard deviation of the collected data is 2.05%. In addition, all junctions are within 10 %.

To further investigate whether the reproducibility can be improved, the junctions were divided into two parts; small junctions (A$\leq$ 3.27μm^2) and large junctions (A$\geq$ 3.27μm^2). Histograms for these two subgroups of junctions are presented in Fig. 5.6 b). The standard deviations of these are 2.33% and 1.48%, respectively, indicating (not surprisingly) that the larger junctions tend to be more reproducible.

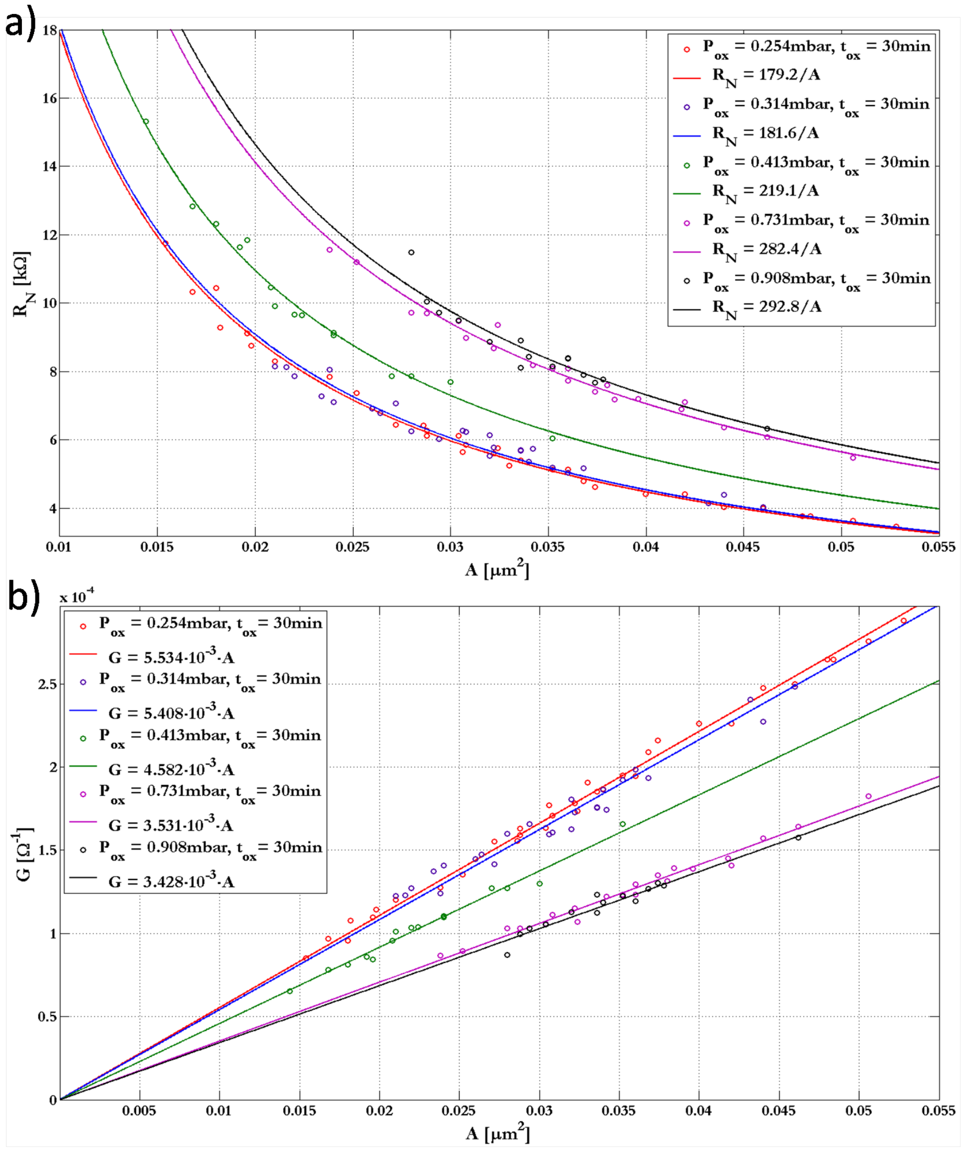

Figure 5.5: *a) The measured R_N for 110 pairs of transmon junctions evaporated using static oxidation in the Plassys for five different P_{ox}. **b)** The corresponding conductance $G = R_N^{-1} = \sigma A$ of the measured R_N in a).*

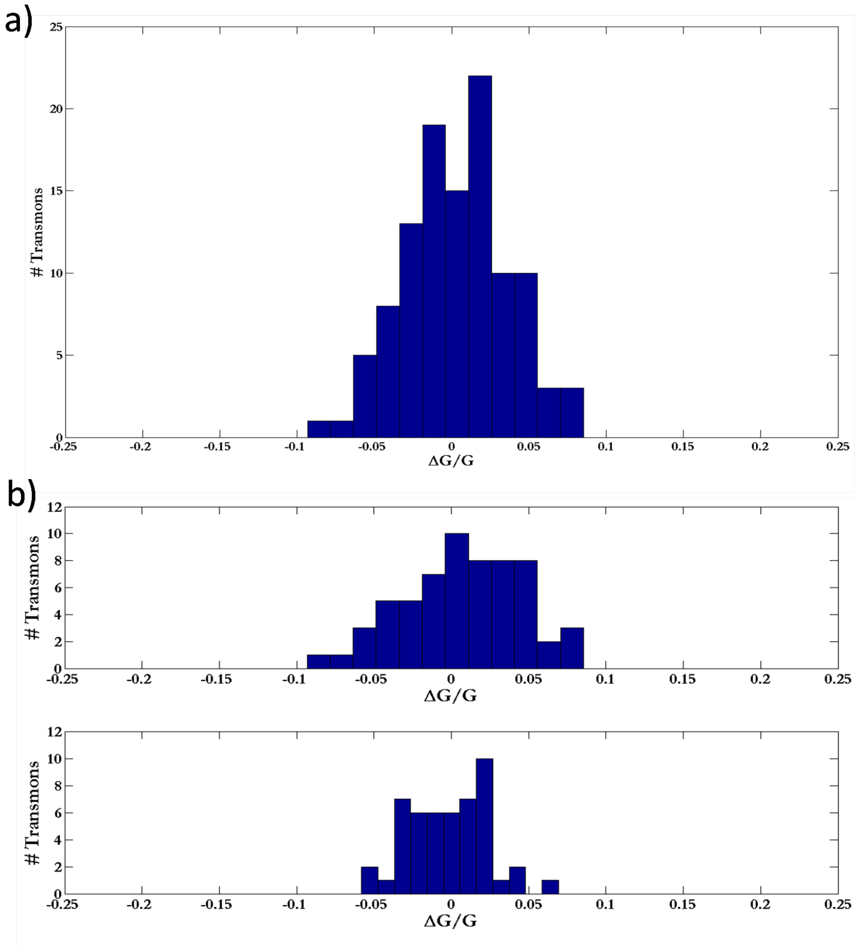

Figure 5.6: ***a)*** *Histogram of the deviation in conductance* $\Delta G/G$ *for all 110 transmons fabricated in the Plassys. The standard deviation of the data is 2.05 %. All samples have deviations within -9 % to +8 %.* ***b)*** *Histograms of the deviation in conductance* $\Delta G/G$ *for small transmon junctions (top plot) and large transmon junctions (bottom plot). The standard deviation is 2.33 % for the small junctions and 1.48 % for the large junctions. From the histograms it is clear that the small junctions tend to deviate more than the larger.*

5.3 Required transmon area

In order to measure the level of optimization for the transmon in terms of its physical size, a representative figure of merit needs to be introduced. In Fig. 5.7, the transmon area is introduced as the total area of the outer borders of the transmon.

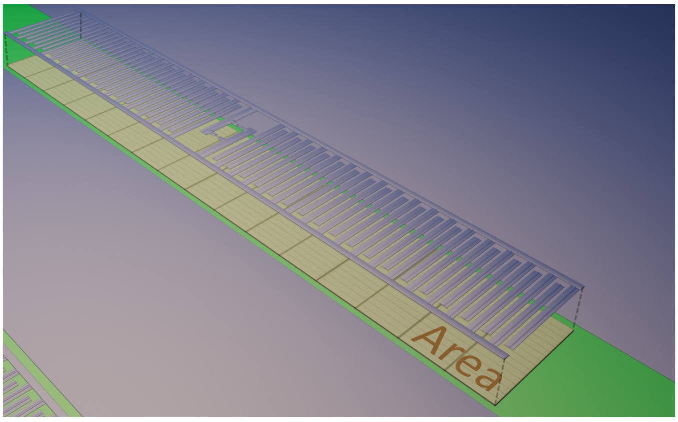

Figure 5.7: *The transmon area as the projection of the outer boundary of the transmon down in the wafer.*

The measured shunt capacitances and normal state resistances of the junctions can now be related to this required area needed for the specific design of fingers in order to obtain a plasma frequency of 6 GHz. However, since the gate capacitance C$_g$ and junction capacitance C$_J$ remain unknown until the transmon has been measured inside the cavity, values of these has been put to 0.1·C$_s$ and 1 fF, respectively. The equation of the linear fit C$_s = 0.5 \cdot 10^{-15} N$ is first used to calculate the shunt capacitance as a function of the number of fingers. In turn, for the finger design at hand it is easy to calculate the length of the transmon L = 2N + 6 where each period of finger + gap is 2 μm and the center part of the transmon is 6 μm.

As described in the simulations, it is not the choice of shunt capacitance nor junction sizes that set the plasma frequency but the combination of the two. Thus, by fixing the plasma frequency at *e.g.* $\nu_p = 6$ GHz, the shunt capacitance can be connected to an area of the transmon and then the needed normal state resistances can be plotted as a function of the area. The relation between R_N and C_Σ can be derived from the plasma frequency relation (2.6)

$$6 \cdot 10^9 = \sqrt{\frac{\Delta e}{2hR_N C_\Sigma}} \quad \rightarrow \quad R_N = \frac{\Delta e}{72 \cdot 10^{18} h C_\Sigma} \tag{5.5}$$

From the limit conditions of $E_J/E_C = 20$ and $E_J/E_C = 100$, the corresponding values of $R_N|_{E_J/E_C=20} = 16.49$ kΩ and $R_N|_{E_J/E_C=100} = 7.314$ kΩ were found. In Fig. 5.8, C_Σ and R_N are plotted as function of the transmon area along with the limiting values marked with the red square.

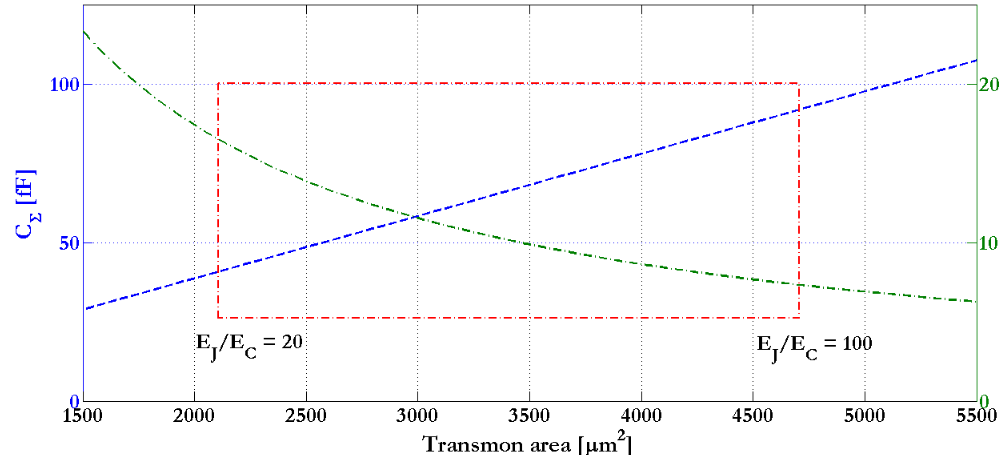

Figure 5.8: *The total capacitance and normal state resistance as function of the transmon area at $\nu_p = 6$ GHz. The red square represents the limits of the transmon regime ($20 \leq E_J/E_C \leq 100$).*

5.4 Predictability of the transmon plasma frequency

The acquired result for the standard deviation of the histogram for the larger half of the transmon junctions can now be translated into a value for the predictability of the plasma frequency. Recall the expression for the plasma frequency of the transmon

$$\nu_p = \frac{\sqrt{8E_J E_C}}{h} \tag{5.6}$$

where the two energies are given as

$$E_J = \frac{h}{4e^2} \cdot \frac{\Delta}{2R_N} = \frac{h\Delta}{8e^2 R_N} \qquad E_C = \frac{e^2}{2C_\Sigma} \tag{5.7}$$

Substitution of (5.7) into the plasma frequency (5.6), the energy separating the ground state and the first excited state can be written as

$$E_{01} = \sqrt{\frac{\Delta}{2hR_N C_\Sigma}} - \frac{e^2}{2C_\Sigma} \tag{5.8}$$

The mean error of the qubit frequency can now be calculated from the following equation

$$|\delta\nu_p| = \left|\frac{\partial\nu_p}{\partial R_n}\right| \cdot |\delta R_n| + \left|\frac{\partial\nu_p}{\partial C_\Sigma}\right| \cdot |\delta C_\Sigma| + \left|\frac{\partial\nu_p}{\partial\Delta}\right| \cdot |\delta\Delta| \approx \left|\frac{\partial\nu_p}{\partial R_n}\right| \cdot |\delta R_n| \tag{5.9}$$

where $|\delta R_n|$, $|\delta C_\Sigma|$, and $|\delta\Delta|$ represent the errors of the different parameters. Since the shunt capacitance of the transmon is very large as compared to the dimensions of its junctions, its uncertainty is set only by the lithography and can be neglected in this context. In addition, by assuming that the Al is clean and evaporated under similar conditions also this contribution is neglected. Thus, by putting $|\delta R_n| \gg |\delta C_\Sigma|, |\delta\Delta|$ following is obtained

$$\left|\frac{\partial\nu_p}{\partial R_n}\right| = \left|\sqrt{\frac{\Delta}{hC_\Sigma}} \cdot - \left(\frac{R_N^{-3/2}}{2}\right)\right| = \left|-\frac{1}{2R_N} \cdot \nu_p\right| = \frac{\nu_p}{2R_N} \tag{5.10}$$

Thus, substitution of (5.10) into (5.9), the relation between the errors can be expressed

$$\delta\nu_p = \frac{\delta R_N}{2R_N} \cdot \nu_p \rightarrow \frac{\delta R_N}{R_N} = \frac{1}{2} \cdot \frac{\delta\nu_p}{\nu_p} \tag{5.11}$$

Finally, the result from the standard deviation $\frac{\delta R_N}{R_N} = 1.48\%$ can be implemented, giving

$$\frac{\delta\nu_p}{\nu_p} = \frac{1}{2} \cdot 1.48 = 0.74\% \tag{5.12}$$

For a qubit frequency of 6 GHz, this means a frequency uncertainty of 44.4 MHz.

Chapter 6

Conclusions and outlook

In this thesis, a quantitative investigation of the predictability of the plasma frequency of the transmon qubit has been carried out. The qubit frequency depends on the shunt capacitance C_s, the normal state resistance R_N and the superconducting gap Δ. We have investigated the the first two of these. The results indicate that high predictability, with standard deviations below two percent for resistance, is obtainable if the junction area of the Josephson junctions in the qubit are slightly scaled up. However, as there are many parameters to consider during fabrication, this standard deviation could probably be decreased further. One parameter which was held constant throughout all fabrication was the rate of deposition of Al in the Plassys. Since the grain size of Al should vary with this rate, it seems likely that also the predictability of the area of the junction would. This could be experimentally investigated further.

Another important factor that needs to be investigated and further improved is the yield of the transmon junctions as this would be a limiting factor when fabricating scaled up systems. However, it is not yet clear whether the low yield ($\approx 50\%$) is due to the actual junctions or problems with the Al/Au interface on the test structures.

So far, only the largest of the three contributions to the total capacitance C_Σ has been measured, namely the shunt capacitance C_s. A natural next step would therefore be to assemble all these subsystems and fabricate transmons coupled to a tunable resonator for measurements in a ^{4}He-^{3}He dilution refrigerator at temperatures around 50mK. Then, a feedback on the predictability of $\mathrm{E}_J(\mathrm{R}_N)$ would be possible from a spectroscopy measurement. In addition, when E_J has been extracted, the two other contributions to C_Σ could be identified by subtracting the now known shunt capacitance. Using these values, a participation ratio analysis could be done where the quality factors of different parts of the system are investigated in order to analyze where the energy of the system is dissipated.

In a longer perspective, if the plasma frequencies of the qubits could be effectively predicted at the fabrication stage, a system consisting of a larger number of transmons coupled to the same tunable cavity could be realized. With a small error in the plasma frequency, the transmons could be placed more dense in frequency, allowing for more qubits within the tuning range of the cavity.

Appendix A

Recipe for fabrication

1. **Cleaning the wafer**
    - 1165 Remover, $60 - 70$°C, 10 min
    - Ultrasonic bath, P = 100%, 1 min
    - IPA bath, $t_{circ} = 2min$
    - QDR bath
2. **Photolithography to define large features**
    - Stripping plasma etching, 1 min, 250W, 40 sccm O_2
    - Spin HMDS Primer, 3000 rpm, 1 min, $t_{acc} = 1.5$ s
      Softbake 1 min, 110 °C
    - Spin LOR3B, 3000 rpm, 1 min, $t_{acc} = 1.5$ s ($\approx$350nm)
      Softbake 5 min, 200 °C
    - Spin S1813, 3000 rpm, 1 min, $t_{acc} = 1.5$ s ($\approx$150nm)
      Softbake 2 min, 110 °C
    - Expose, (DUV 400 nm), 6 W/cm^2, $t_{exp} = 10$ s, Hard Contact mode
    - Develop, MF319, 30 s (Lift up and rinse after 15 s.)
3. **Deposition of gold contacts**
    - Ashing in O_2-plasma, 30 s, 50 W
    - Electron beam evaporation, (Baltzer BAK600), $P_{ch} \leq 10^{-7}$mbar
      Sticking layer: 30 Å of Ti, 2 Å/s
      Contact layer: 800 Å of Au, 5 Å/s
      Stopping layer: 100 Å pf Pd, 2 Å/s

- Lift-off excess metals, 1165 Remover, $60-70$°C, $\approx$50 min

4. **Semi-dicing of the wafer from the backside**

   - Spin protective resist layer, S1813, 3000 rpm, 1 min, $t_{acc} = 1,5$s
     Softbake 3 min, 110 °C
   - Semi-dice the wafer from the backside using Loadpoint MicroAce 3+ Dicing saw. Leave approximately 170 μm of the wafer. Divide the wafer into chips of dimension 8,7 × 4,5 mm.
   - Remove protective resist, 1165 Remover, $60-70$°C, $\approx$ 10 min
     Rinse gently with IPA

5. **Electron beam lithography to define small features**

   - Spin Nano Copolymer in Ethyl Lactate 10%, 500 rpm, $t_{acc} = 2$ s for 5 s, spin 2000 rpm, $t_{acc} = 0,5$ s for 45 s (layer thickness $\approx$ 570 nm)
     Softbake 5 min, 170 °C
   - Spin ZEP 520A 1:1 Anisole, 3000 rpm, $t_{acc} = 0,5$ s, spin 45 s (layer thickness $\approx$125 nm)
     Softbake 5 min, 160 °C
   - Expose, JEOL JBX-9300FS, 100kV, dose 150 μC/cm^2
   - Develop top layer of ZEP 520A, O-xylene, 2 min
     Rinse in isopropyl alcohol (IPA)
   - Develop bottom layer Nano Copolymer, H_2O:IPA 1:4, 4 min 30 s (undercut $\geq 0,2\mu$m)

6. **Two-angle evaporation of Josephson junctions**

   - Ashing in O_2-plasma, 10 s, 50 W
   - Electron beam evaporation in the Plassys:
   - Evaporate bottom electrode, 40 nm, Rate: 5 Å/s, $\alpha = 31°$
   - Dynamic oxidation, $P_{ox} = 0,2$ mbar, $t_{ox} = 30$ min
   - Evaporate top electrode, 50 nm, Rate: 5 Å/s, $\alpha = -31°$
   - Lift-off excess Al, 1165 Remover, $60-70$°C, $\approx$20 min
     Rinse in isopropyl alcohol (IPA) and blowdry with N_2-gun

Appendix B

Design guide for SQUID junctions

The intention of this guide is to provide an easy way of fabricating tunnel junctions for SQUIDS with a desired normal state resistance R$_N$.

In Fig. B.1, the results from four Plassys evaporations using the oxidation parameters: $t_{ox} = 30$ min, $P_{ox} = 0.2$ mbar dynamic. Note that R_N is plotted as a function of the designed junction width as oppose to previous plots where the area is found on the x-axis. The reason for this is to make it easier to reproduce. For example, let us pretend that we want to design a SQUID with a $R_N = 160\ \Omega$.

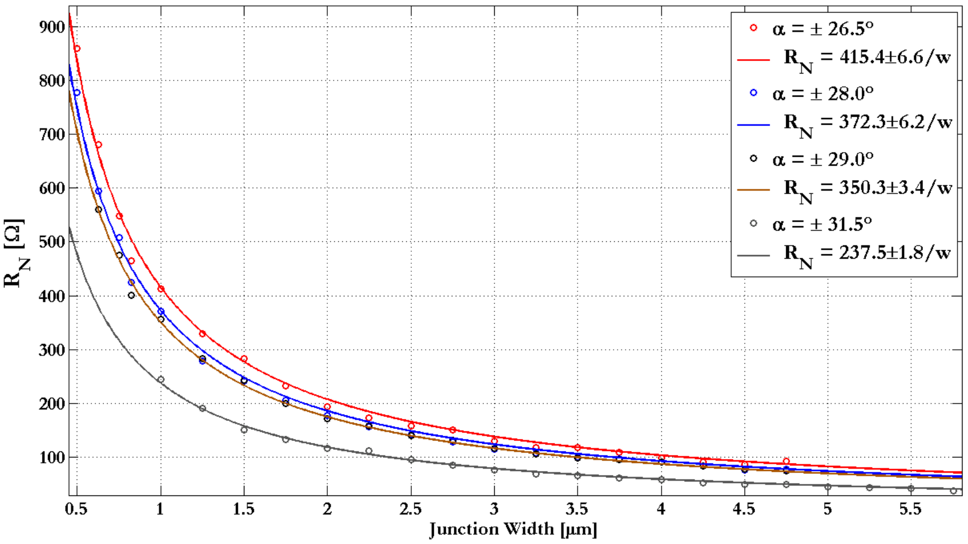

Figure B.1: *Junction resistance as function of the junction width for four SQUID samples evaporated from four different angles*

1. First, chose one of the fitting functions that covers the resistance. For example the grey curve given by

$$R_N = \frac{237.5}{w} \tag{B.1}$$

where w is the designed junction width. For a desired resistance of R_N=160 Ω, the following width is needed

$$w = \frac{237.5}{160} \approx 1.48\mu m \tag{B.2}$$

2. Now, make your AutoCAD file for the e-beam according to the dimensions in Fig. B.2. The length of the resist bridge should be 0.250 μm.

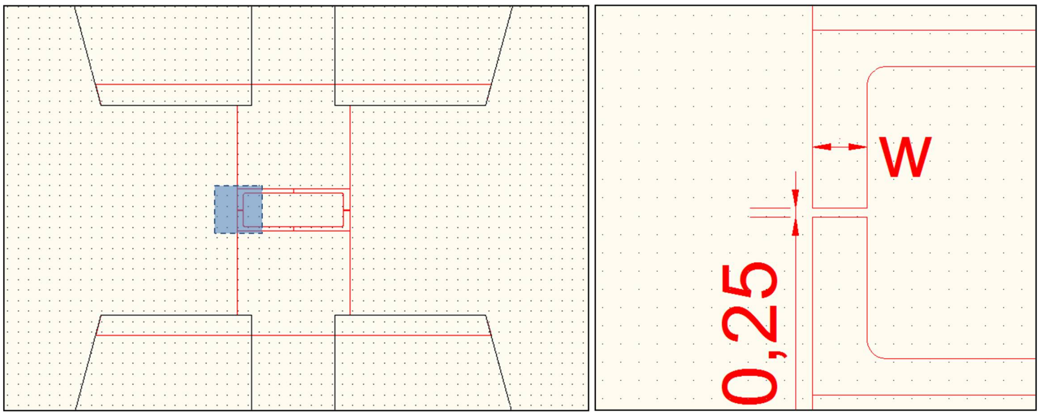

Figure B.2: *The AutoCAD designed used for the SQUID junctions. W represent the width of the junction while the length of the junction is 0.250μm.*

3. Use the following e-beam recipe:

   - Spin Nano Copolymer in Ethyl Lactate 10%, 500 rpm, t_{acc} = 2 s for 5 s, spin 2000 rpm, $t_{acc} = 0,5$ s for 45 s (layer thickness 570 nm)
     Softbake 5 min, 170 °C
   - Spin ZEP 520A 1:1 Anisole, 3000 rpm, $t_{acc} = 0,5$ s, spin 45 s (layer thickness 125 nm)
     Softbake 5 min, 160 °C
   - Expose, JEOL JBX-9300FS, 100kV, dose 150 μC/cm^2
   - Develop top layer of ZEP 520A, O-xylene, 2 min
     Rinse in isopropyl alcohol (IPA)

- Develop bottom layer Nano Copolymer, H_2O:IPA 1:4, 4 min 30 s (undercut $\geq 0,2\mu$m)

4. Use the following two angle evaporation recipe:

   - Ashing in O_2-plasma, 10 s, 50 W
   - Electron beam evaporation in the Plassys:
   - Evaporate bottom electrode, 40 nm, Rate: 5 Å/s, $\alpha = 31.5°$
   - Dynamic oxidation, $P_{ox} = 0,2$ mbar, $t_{ox} = 30$ min
   - Evaporate top electrode, 50 nm, Rate: 5 Å/s, $\alpha = -31.5°$
   - Lift-off excess Al, 1165 Remover, $60 - 70$°C, ≈20 min
     Rinse in isopropyl alcohol (IPA) and blowdry with N_2-gun

Bibliography

[1] R.P. Feynman, *Simulating Physics with Computers*, International Journal of Theoretical Physics **21**: 467–488 (1982)

[2] T. Yamamoto, Y. A. Pashkin, O. Astafiev, Y. Nakamura, and J. S. Tsai, Nature **425**, 941 (2003)

[3] M. Stefien, M. Ansmann, R. C. Bialczak, N. Katz, E. Lucero, R. McDermott, M. Neeley, E. M. Weig, A. N. Cleland, and J. M. Martinis, Science **313**, 1423 (2006)

[4] D. Leibfried, R. Blatt, C. Monroe, and D. Wineland, Reviews of Modern Physics **75**, 281, (2003)

[5] J. Koch, T.M. Yu, J. Gambetta, A.A. Houck, D.I. Schuster, J. Majer, M.H. Devoret, S.M. Girvin, R.J. Schoelkopf,*Charge-insensitive qubit design derived from the Cooper pair box*, Phys. Rev. A **76**, 042319 (2007)

[6] A. Blais, R.S. Huang, A. Wallraff, S. M. Girvin, and R. J. Schoelkopf, PRA **69**, 062320 (2004)

[7] S. Haroche, J-M. Raimond *Exploring the Quantum: Atoms, Cavities, and Photons*, Oxford University Press Inc., New York, USA, (2006)

[8] M.A. Nielsen, I.L. Chuang, *Quantum computation and quantum information*, Chapter 1, Cambridge University Press, Cambridge, England, (2000)

[9] K.H.Onnes, *The Superconductivity of Mercury*, Comm. Phys. Lab. Univ. Leiden **122**, 251 (1911)

[10] R.P. Feynman, *Lectures on physics Vol III*, Pearson Addison-Wesley, (2006)

[11] B.D. Josephson, *Possible new effects in superconductive tunnelling*, Phys. Lett. **1**, 251 (1962)

[12] M. Tinkham, *Introduction to superconductivity*, Dover Publications, inc., New York, 2^{nd} edition, (1996)

[13] T. van Duzer, C.W. Turner *Principles of superconductive devices and circuits*, Prentice Hall PTR, 2^{nd} edition, (1999)

[14] M. Büttiker, Phys. Rev. B **33**, 3020 (1986)

[15] Y. Nakamura, Y. A. Pashkin, J. S. Tsai,*Coherent control of macroscopic quantum states in a single-Cooper-pair box*, Nature **398**, (1999)

[16] K. Bladh, T. Duty, D. Gunnarsson, P. Delsing,*The single Cooper-pair box as a charge qubit*, New Journal of Physics 7, **180**, (2005)

[17] A.R. Lide, *Handbook of chemistry and physics*, CRC Press LLC, 85^{th} edition, (2004)

[18] J. Bardeen, L. N. Cooper, and J. R. Schrieffer, *Theory of Superconductivity*, Phys. Rev. **108**, 1175 (1957)

[19] D. Vion, A. Aassime, A. Cottet, P. Joyez, H. Pothier, C. Urbina, D. Esteve, M. H. Devoret, *Manipulating the Quantum State of an Electrical Circuit*, Science **296**, 886 (2002)

[20] H.Haken, H.C. Wolf, *The physics of atoms and quanta: Introduction to experiments and theory*, 7^{th} edition, Springer, New York, USA, (2005)

[21] C.P. Wen,*Coplanar Waveguide: a surface strip transmission line for nonreciprocal gyromagnetic device application*, IEEE Trans. on MTT, **1087**, Dec (1969)

[22] A. Myrin, *Master of Science Thesis* (Not yet published), (2010)

[23] M. Sandberg, *Fast-tunable resonators and quantum electrical circuits*,PhD thesis, Chalmers University of Technology, (2009)

[24] F. Persson, *Fast dynamics and measurements of single-charge devices*, PhD thesis, Chalmers University of Technology, (2010)

[25] N.S. Rainee, *Coplanar Waveguide Circuits, Components, and Systems*, John Wiley & Sons, New York, USA, (2001)

[26] D.A. Neamen, *Semiconductor Physics and Devices: Basic Principles*, McGraw-Hill, 3^{rd} edition, (2003)

[27] S.S. Gevorgian, T. Martinsson, P.L.J. Linnér, E.L. Kollberg, *CAD Models for Multilayered Substrate Interdigital Capacitors*, IEEE Transactions on Microwave Theory and Techniques **44**, no. 6 June, (1996)

[28] Oxford Instruments webpage *url: http://www.oxford-instruments.com/products/low-temperature/3he-refrigerators/helioxvl/Pages/helioxvl.aspx* retrieved 20100402

[29] A. A. Houck, J. Koch, M. H. Devoret, S. M. Girvin, R. J. Schoelkopf, *Life after charge noise: recent results with transmon qubits*, Quantum Information Processing **8** 2-3, (2009)

[30] R.H. Koch, D.P. DiVincenzo, J. Clarke, *Model for 1/f flux noise in squids and qubits*, Phys. Rev. Lett. **98**, 267003, (2007)

[31] C.C. Gerry, P.L. Knight, *Introductory Quantum Optics*, Cambridge University Press, Cambridge, England, (2005)

[32] J. Clarke, F.K. Wilhelm, *Superconducting quantum bits*, Nature **453**, 1031, (2008)